

# Fully general relativistic simulation of coalescing binary neutron stars: Preparatory tests

Masaru Shibata

*Department of Physics, University of Illinois at Urbana-Champaign, Urbana, IL 61801, USA*  
and

*Department of Earth and Space Science, Graduate School of Science, Osaka University,  
Toyonaka, Osaka 560-0043, Japan*

We present our first successful numerical results of 3D general relativistic simulations in which the Einstein equation as well as the hydrodynamic equations are fully solved. This paper is especially devoted to simulations of test problems such as spherical dust collapse, stability test of perturbed spherical stars, and preservation of (approximate) equilibrium states of rapidly rotating neutron star and/or corotating binary neutron stars. These test simulations confirm that simulations of coalescing binary neutron stars are feasible in a numerical relativity code. It is illustrated that using our numerical code, simulations of these problems, in particular those of corotating binary neutron stars, can be performed stably and fairly accurately for a couple of dynamical timescales. These numerical results indicate that our formulation for solving the Einstein field equation and hydrodynamic equations are robust and make it possible to perform a realistic simulation of coalescing binary neutron stars for a long time from the innermost circular orbit up to formation of a black hole or neutron star.

04.25.Dm, 04.30.-w, 04.40.D

## I. INTRODUCTION

The coalescence of binary neutron stars is one of the most promising sources for planned kilometer size laser interferometers such as LIGO [1,2], VIRGO [3], GEO [4] and TAMA [5], which will be in operation within the next five years. When a signal of gravitational waves is detected from binary neutron stars, it will provide not only the first chance to observe highly relativistic objects in a dynamical motion, but also a wide variety of physical information of binary neutron stars including their mass, spin, radius and innermost stable circular orbit (ISCO) [2]. The signal of gravitational waves from such compact objects will be analyzed using matched filter techniques to extract the physical information. To apply this technique, theoretical templates of gravitational waveforms are needed [2]. This fact has motivated an intense theoretical effort for preparing such templates.

The orbital evolution of binary neutron stars can be divided into three stages; inspiraling stage, intermediate stage, and dynamical stage. For the study of the inspi-

raling stage in which their orbital radius is much larger than the stellar radius ( $R$ ) and neutron stars are in quasi-periodic states gradually decreasing the orbital radius as a result of emission of gravitational waves, a post Newtonian approximation is powerful. Much effort has been paid for obtaining a template of high-order post Newtonian corrections, providing many recent satisfactory results [6].

When the orbital radius of the binary neutron stars decreases to a few  $R$  as a consequence of gravitational wave emission, the effect of the multipole moments of each neutron star induced by the tidal field from the companion star cannot be ignored. Even at this stage, the emission timescale of gravitational waves is still much longer than the orbital period. In this intermediate stage between the inspiraling and dynamical stages, the binary can be assumed to be in a quasi-hydrostatic equilibrium state. For the theoretical study, it is adequate to obtain the quasi-equilibrium configuration taking into account the effects of the deformation of the neutron stars but assuming that emission of gravitational waves is negligible.

In this research field, an effort has been paid recently, yielding gradually successful results [7–9].

With the further emission of gravitational waves, the binary neutron stars approach the ISCO. Upon reaching the ISCO, they behave in a dynamical manner. For the theoretical study of such a dynamical stage, no approximation for general relativity is applicable because the system is dominated by highly general relativistic gravity and hydrodynamic effect. In this respect, numerical relativistic simulation is the only promising method for the theoretical study.

Numerical relativity also plays an important role for a theoretical study on the origin of  $\gamma$ -ray bursts (GRBs) because the short rise times of the bursts imply that their central sources have to be relativistic objects [10]. Recently, at least some of GRBs have been turned out to be of cosmological origin [11]. In cosmological GRBs, the central sources must provide a large amount of the energy  $\gtrsim 10^{51}$  ergs in a very short timescale of order msec–sec. It has been suggested that the merger of binary neutron stars could be a likely candidate for the powerful central source [10]. The typical scenario is based on the assumption that a system composed of a rotating black hole and a surrounding massive disk is formed after the merger. To clarify whether such scenario is correct, numerical simulations have been performed including effects of emission by gravitational radiation and/or neutrino and adopting a realistic equation of state for the neutron stars [12]. So far, the results in the numerical simulations have not supported such scenario [12]; i.e., the evidence that the massive disk is formed around the black hole has not been found. However, all the simulations have been performed in the Newtonian or post Newtonian approximations. Needless to say, general relativistic effects can play a very important role in the mergers between two neutron stars. To obtain the true answer, therefore, a fully general relativistic simulation is necessary.

Much effort has been paid toward constructing a reliable numerical relativity code which makes it possible to clarify the evolution of merging binary neutron stars

and the gravitational waveform emitted by them. Several projects in the world such as those by Nakamura and Oohara [13,14] and by Washington University group [15] are in progress, but no satisfactory results have been reported yet.

To perform numerical simulation of coalescing binary neutron stars for a long time from the ISCO to formation of a black hole or new neutron star, it is necessary to choose appropriate gauge conditions which make it possible to perform the long-timescale simulation stably and to extract gravitational waves accurately. In a previous paper [16], we performed fully general relativistic simulations of coalescing binary clusters using collisionless particles as the matter source of the Einstein equation. For the simulation, we used the approximate minimum distortion gauge and approximate maximal slicing conditions as the spatial and time coordinate conditions (see Sec II.B). We found that these gauge conditions are robust enough to allow for stable and long-timescale simulations of merging clusters as well as for the fairly accurate extraction of gravitational waves. In this paper, we perform simulations adopting the same gauge conditions and formulation for the Einstein equation and incorporating a solver of the relativistic hydrodynamic equations. We demonstrate the robustness of our formulation presenting successful numerical results of 3D hydrodynamic simulations.

In particular, this paper is devoted to simulations of test problems. The purpose here is to ensure that numerical simulations of coalescing binary neutron stars for a long timescale from the ISCO to the formation of a black hole or neutron star are feasible in our formulation and numerical code. The test problems presented in this paper are a spherical dust collapse, stability test of spherical stars in equilibrium states, excitation of quadrupole oscillations of perturbed spherical stars, preservation of stable rapidly rotating stars in equilibrium states, and preservation of corotating binary neutron stars in an approximate quasi-equilibrium orbit. We show that stable and fairly accurate simulations for these test problems are feasible

with our code, indicating the feasibility of forthcoming realistic simulations of coalescing binary neutron stars.

The paper is organized as follows. In Sec. II, our formulation for solving the Einstein field equations as well as relativistic hydrodynamic equations are described. We also describe the gauge conditions and the numerical method employed in this paper briefly. In Sec. III, we describe test problems which should be carried out to check the accuracy and performance of a numerical relativity code for solving the coupled equations composed of the Einstein and hydrodynamic equations. Then, we present the numerical results for the test simulations. In Sec. IV, we present numerical results of merger of corotating binary neutron stars as an example. Sec. V is devoted to a summary. Throughout this paper, we adopt the units  $G = c = M_{\odot} = 1$  where  $G$ ,  $c$  and  $M_{\odot}$  denote the gravitational constant, speed of light and the solar mass, respectively. Hence, the units of length, time, mass, and density are 1.477km,  $4.927 \times 10^{-6}$ sec,  $1.989 \times 10^{33}$ g, and  $6.173 \times 10^{17}$ g/cm<sup>3</sup>. Latin and Greek indices denote spatial components (1–3) and spacetime components (0–3), respectively. As spatial coordinates, we use the Cartesian coordinates  $x^k = (x, y, z)$  with  $r = \sqrt{x^2 + y^2 + z^2}$ .  $\delta_{ij} (= \delta^{ij})$  denotes the Kronecker delta.

## II. FORMULATION

### A. Basic equations

Our code solves the coupled equations of the Einstein equation and relativistic hydrodynamic equations. Our formulation for solving the Einstein equation has been described in detail in previous papers [17,18,16]. Since we adopt the same formulation only changing the matter source, we here only review the basic equations.

We write the line element in the form

$$ds^2 = g_{\mu\nu}dx^{\mu}dx^{\nu} = (-\alpha^2 + \beta_k\beta^k)dt^2 + 2\beta_i dx^i dt + \gamma_{ij}dx^i dx^j, \quad (2.1)$$

where  $g_{\mu\nu}$ ,  $\alpha$ ,  $\beta^i$  ( $\beta_i = \gamma_{ij}\beta^j$ ), and  $\gamma_{ij}$  are the 4D metric, lapse function, shift vector, and 3D spatial metric,

respectively. Following previous papers [17,18,16], we define the quantities to be solved in numerical computation as

$$\gamma = \det(\gamma_{ij}) \equiv e^{12\phi}, \quad (2.2)$$

$$\tilde{\gamma}_{ij} \equiv e^{-4\phi}\gamma_{ij} \text{ (i.e., } \det(\tilde{\gamma}_{ij}) = 1\text{)}, \quad (2.3)$$

$$\tilde{A}_{ij} \equiv e^{-4\phi}\left(K_{ij} - \frac{1}{3}\gamma_{ij}K_k^k\right), \quad (2.4)$$

where  $K_{ij}$  is the extrinsic curvature,  $K_k^k$  its trace. We note that indices of  $\tilde{A}_{ij}$  and/or  $\tilde{A}^{ij}$  are raised and lowered in terms of  $\tilde{\gamma}_{ij}$  and  $\tilde{\gamma}^{ij}$ . In the numerical computation, we solve for  $\tilde{\gamma}_{ij}$ ,  $\tilde{A}_{ij}$ ,  $\phi$  and  $K_k^k$  instead of  $\gamma_{ij}$  and  $K_{ij}$ . Hereafter, we use  $\nabla_{\mu}$ ,  $D_i$  and  $\tilde{D}_i$  as the covariant derivatives with respect to  $g_{\mu\nu}$ ,  $\gamma_{ij}$  and  $\tilde{\gamma}_{ij}$ , respectively.

As the matter source of the Einstein equation, we adopt a perfect fluid. In this case, the energy momentum tensor is written as

$$T_{\mu\nu} = (\rho + \rho\varepsilon + P)u_{\mu}u_{\nu} + Pg_{\mu\nu}, \quad (2.5)$$

where  $\rho$ ,  $\varepsilon$ ,  $P$ , and  $u_{\mu}$  are the rest mass density, specific internal energy density, pressure and four-velocity, respectively. Hereafter, we assume an equation of state in the form,  $P = (\Gamma - 1)\rho\varepsilon$ , where  $\Gamma$  is a constant.

The hydrodynamic equations are composed of the continuity, Euler and energy (or entropy) equations, which are derived from

$$\nabla_{\mu}(\rho u^{\mu}) = 0, \quad (2.6)$$

$$\gamma_i^{\mu}\nabla_{\nu}T_{\mu}^{\nu} = 0, \quad (2.7)$$

$$u^{\mu}\nabla_{\nu}T_{\mu}^{\nu} = 0. \quad (2.8)$$

We write their explicit forms as

$$\partial_t\rho_* + \partial_i(\rho_*v^i) = 0, \quad (2.9)$$

$$\begin{aligned} \partial_t(\rho_*\hat{u}_k) + \partial_i(\rho_*\hat{u}_kv^i) \\ = -\alpha e^{6\phi}\partial_kP - \rho_*\left[w\hat{h}\partial_k\alpha - \hat{u}_j\partial_k\beta^j + \frac{\alpha e^{-4\phi}\hat{u}_i\hat{u}_j}{2wh}\partial_k\tilde{\gamma}^{ij} - \frac{2\alpha h(w^2 - 1)}{w}\partial_k\phi\right], \end{aligned} \quad (2.10)$$

$$\partial_t e_* + \partial_i(e_*v^i) = 0, \quad (2.11)$$

where  $\partial_{\mu} = \partial/\partial x^{\mu}$ ,  $\rho_* = \rho w e^{6\phi}$ ,  $h = 1 + \varepsilon + P/\rho$ ,  $w = \alpha u^0$ ,  $\hat{u}_k = h u_k$ ,  $e_* = (\rho\varepsilon)^{1/\Gamma} w e^{6\phi}$ , and  $v^i (\equiv u^i/u^0)$  is written as

$$v^i = -\beta^i + \frac{\alpha\tilde{\gamma}^{ij}\hat{u}_j}{whe^{4\phi}}. \quad (2.12)$$

In numerical simulation, we solve Eqs. (2.9)–(2.11) to evolve  $\rho_*$ ,  $\hat{u}_k$  and  $e_*$ .

The volume integral of  $\rho_*$  in the three hypersurface,

$$M_* \equiv \int d^3x \rho_*, \quad (2.13)$$

denotes the total rest mass of the system, which should be conserved with time. Although the equation for  $e_*$  has the same form as that for  $\rho_*$ , the volume integral of  $e_*$  is not conserved in the presence of shocks. This implies that using Eq. (2.11) we cannot obtain the correct solution when shock is formed. Thus, the artificial viscosity terms are added in Eqs. (2.10) and (2.11) for some problems in which shock is formed and plays an important role during the evolution of the system (see Appendix A).

Once  $\hat{u}_i$  is obtained,  $w(= \alpha u^0)$  is determined from the normalization relation of the four-velocity, which can be written as

$$w^2 = 1 + e^{-4\phi}\tilde{\gamma}^{ij}\hat{u}_i\hat{u}_j \left[ 1 + \frac{\Gamma e_*^\Gamma}{\rho_* (w e^{6\phi})^{\Gamma-1}} \right]^{-2}. \quad (2.14)$$

The Einstein equation is split into the constraint and evolution equations. The Hamiltonian and momentum constraint equations are written as

$$R_k^k - \tilde{A}_{ij}\tilde{A}^{ij} + \frac{2}{3}(K_k^k)^2 = 16\pi E, \quad (2.15)$$

$$D_i\tilde{A}^i_j - \frac{2}{3}D_jK_k^k = 8\pi J_j, \quad (2.16)$$

where

$$E \equiv T^{\mu\nu}n_\mu n_\nu = \rho_* h w e^{-6\phi} - P, \quad (2.17)$$

$$J_i \equiv -T^{\mu\nu}n_\mu\gamma_{\nu i} = \rho_* e^{-6\phi}\hat{u}_i, \quad (2.18)$$

$n_\mu = (-\alpha, 0)$ , and  $R_{ij}$  is the Ricci tensor with respect to  $\gamma_{ij}$ .

Following our previous works, we write the evolution equations for the geometric variables in the form [18,16]

$$(\partial_t - \beta^l\partial_l)\tilde{\gamma}_{ij} = -2\alpha\tilde{A}_{ij} + \tilde{\gamma}_{ik}\beta^k_{,j} + \tilde{\gamma}_{jk}\beta^k_{,i} - \frac{2}{3}\tilde{\gamma}_{ij}\beta^k_{,k}, \quad (2.19)$$

$$(\partial_t - \beta^l\partial_l)\tilde{A}_{ij} = e^{-4\phi} \left[ \alpha \left( R_{ij} - \frac{1}{3}e^{4\phi}\tilde{\gamma}_{ij}R_k^k \right) \right.$$

$$\left. - \left( D_i D_j \alpha - \frac{1}{3}e^{4\phi}\tilde{\gamma}_{ij}D_k D^k \alpha \right) \right] \\ + \alpha(K_k^k\tilde{A}_{ij} - 2\tilde{A}_{ik}\tilde{A}_j^k) \\ + \beta^k_{,i}\tilde{A}_{kj} + \beta^k_{,j}\tilde{A}_{ki} - \frac{2}{3}\beta^k_{,k}\tilde{A}_{ij} \\ - 8\pi\alpha \left( e^{-4\phi}S_{ij} - \frac{1}{3}\tilde{\gamma}_{ij}S_k^k \right), \quad (2.20)$$

$$(\partial_t - \beta^l\partial_l)\phi = \frac{1}{6} \left( -\alpha K_k^k + \beta^k_{,k} \right), \quad (2.21)$$

$$(\partial_t - \beta^l\partial_l)K_k^k = \alpha \left[ \tilde{A}_{ij}\tilde{A}^{ij} + \frac{1}{3}(K_k^k)^2 \right] \\ - D_k D^k \alpha + 4\pi\alpha(E + S_k^k), \quad (2.22)$$

where  $Q_{,i} = \partial_i Q$  for an arbitrary variable  $Q$ , and

$$S_{ij} \equiv T^{\mu\nu}\gamma_{\mu i}\gamma_{\nu j} = \rho_* e^{-6\phi}(wh)^{-1}\hat{u}_i\hat{u}_j + e^{4\phi}\tilde{\gamma}_{ij}P. \quad (2.23)$$

In calculating  $R_{ij}$  and  $R_k^k$  in Eq. (2.20), we have terms of the type as  $\delta^{kl}\tilde{\gamma}_{ik,lj}$  and  $\delta^{kl}\tilde{\gamma}_{jk,li}$ . For evaluation of such terms, we define the auxiliary variable  $F_i = \delta^{jl}\partial_l\tilde{\gamma}_{ij}$  [19,18,16] and solve the evolution equation

$$(\partial_t - \beta^l\partial_l)F_i = 2\alpha \left\{ f^{kj}\tilde{A}_{ik,j} + f^{kj}_{,j}\tilde{A}_{ik} \right. \\ \left. - \frac{1}{2}\tilde{A}^{jl}h_{lj,i} + 6\phi_{,k}\tilde{A}^k_i - \frac{2}{3}(K_k^k)_{,i} \right\} \\ - 2\delta^{jk}\alpha_{,k}\tilde{A}_{ij} + \delta^{jl}\beta^k_{,l}h_{ij,k} \\ + (\tilde{\gamma}_{il}\beta^l_{,j} + \tilde{\gamma}_{jl}\beta^l_{,i} - \frac{2}{3}\tilde{\gamma}_{ij}\beta^l_{,l})_{,k}\delta^{jk} \\ - 16\pi\alpha J_i, \quad (2.24)$$

where  $h_{ij} = \tilde{\gamma}_{ij} - \delta_{ij}$ , and  $f^{ij} = \tilde{\gamma}^{ij} - \delta^{ij}$ . Then,  $\delta^{kl}\tilde{\gamma}_{ik,lj}$  is evaluated as  $F_{i,j}$ .

We define the total angular momentum of the system as

$$J \equiv \lim_{r \rightarrow \infty} \frac{1}{8\pi} \oint (x\tilde{A}_{yj} - y\tilde{A}_{xj})e^{6\phi} dS^j \\ = \int d^3x e^{6\phi} \left[ xJ_y - yJ_x + \frac{1}{8\pi}(\tilde{A}_y^x - \tilde{A}_x^y) \right. \\ \left. - \frac{1}{16\pi}\tilde{A}_{ij}(x\partial_y - y\partial_x)\tilde{\gamma}^{ij} \right. \\ \left. + \frac{1}{12\pi}(x\partial_y - y\partial_x)K_k^k \right], \quad (2.25)$$

where we use the Gauss's law and Eq. (2.16) to derive the final expression. We also use the following quantity to roughly estimate the angular momentum inside a coordinate radius  $r$  as

$$J(r) = \int_{|x^i| < r} d^3x e^{6\phi}(xJ_y - yJ_x). \quad (2.26)$$

## B. Gauge conditions

As in a previous paper [16], we adopt an approximate maximal slice (AMS) condition and an approximate minimum distortion (AMD) gauge condition as the time and spatial gauge conditions, respectively, for most of the simulations in this paper. In some test simulations carried out in Sec. III, we also use the zero shift vector gauge condition  $\beta^k = 0$  for comparison between two results obtained in different gauge conditions.

To impose the AMS condition, we solve the following parabolic type equation for  $\ln \alpha$  at each time step until an approximate convergence is achieved:

$$\partial_\lambda \ln \alpha = D_k D^k \ln \alpha + (D_k \ln \alpha)(D^k \ln \alpha) - 4\pi(E + S_k^k) - \tilde{A}_{ij} \tilde{A}^{ij} - \frac{1}{3}(K_k^k)^2 + f_\alpha K_k^k \rho_*^{1/2}. \quad (2.27)$$

Here  $\lambda$  denotes a control parameter and  $f_\alpha$  is a constant for which we assign a constant of  $O(1)$ . Assuming that the convergence is achieved and that the right-hand side of Eq. (2.27) becomes zero, the evolution equation for  $K_k^k$  can be written as

$$(\partial_t - \beta^l \partial_l) K_k^k = -f_\alpha \alpha K_k^k \rho_*^{1/2}. \quad (2.28)$$

Thus, if  $K_k^k$  is zero initially and the convergence is completely achieved, the the maximal slice condition  $K_k^k = 0$  is preserved. Even when the convergence is incomplete and  $K_k^k$  deviates from zero, the right-hand side of Eq. (2.28) enforces  $|K_k^k|$  to approach to zero in the local dynamical timescale  $\sim \rho_*^{-1/2}$ . Hence, the condition  $K_k^k = 0$  is expected to be satisfied approximately.

To impose the AMD gauge condition, we solve the following simple elliptic type equations

$$\Delta P_i = S_i, \quad (2.29)$$

$$\Delta \eta = -S_i x^i, \quad (2.30)$$

where  $\Delta$  denotes the Laplacian in the flat 3D space, and

$$S_i \equiv 16\pi\alpha J_i + 2\tilde{A}_{ij}(\tilde{D}^j \alpha - 6\alpha \tilde{D}^j \phi) + \frac{4}{3}\alpha \tilde{D}_i K_k^k. \quad (2.31)$$

From  $P_i$  and  $\eta$ , we determine  $\beta^i$  as

$$\beta^i = \delta^{ij} \left[ \frac{7}{8} P_i - \frac{1}{8} (\eta_{,i} + P_{k,i} x^k) \right]. \quad (2.32)$$

Namely,  $\beta^i$  satisfies an elliptic type equation in the form

$$\delta_{ij} \Delta \beta^i + \frac{1}{3} \beta^k_{,kj} = S_j. \quad (2.33)$$

As we described in a previous paper [16], if an action

$$I = \int d^3x (\partial_t \tilde{\gamma}_{ij})(\partial_t \tilde{\gamma}_{kl}) \tilde{\gamma}^{ik} \tilde{\gamma}^{jl}. \quad (2.34)$$

is minimized with respect to  $\beta^i$ , we obtain the equation of a minimum distortion (MD) gauge condition [20] for  $\beta^i$  as

$$\tilde{\gamma}_{jk} \tilde{D}^i \tilde{D}_i \beta^k + \frac{1}{3} \tilde{D}_j \tilde{D}_i \beta^i + \tilde{R}_{jk} \beta^k = S_j, \quad (2.35)$$

where  $\tilde{R}_{jk}$  is the Ricci tensor with respect to  $\tilde{\gamma}_{ij}$ . Thus, the equation for  $\beta^i$  in the AMD gauge condition is obtained by neglecting coupling terms between  $\beta^i$  and  $h_{ij}$  in Eq. (2.35). Since the neglected terms are expected to be small [16], we can expect that  $I$  is approximately minimized in the AMD gauge condition.

The other benefit in the AMD gauge condition is that  $F_i$  is guaranteed to be small everywhere except in the strong field region just around a highly relativistic object [16]. This implies that a transverse condition,  $\delta^{ij} \partial_i \tilde{\gamma}_{jk} = 0$ , approximately holds for  $\tilde{\gamma}_{ij}$  in the wave zone, helping the accurate extraction of gravitational waves near the outer boundaries of the computational domain.

## C. Initial value formalism

Initial conditions are obtained by solving the constraint equations (2.15) and (2.16). In this paper, we restrict our attention to initial conditions in which  $h_{ij}$  ( $= \tilde{\gamma}_{ij} - \delta_{ij}$ ) = 0 and  $K_k^k = 0$ . Then, the basic equations for obtaining the initial data are the same as those in [18,16] as described below.

Using the conformal factor  $\psi \equiv e^\phi$ ,  $\hat{A}_{ij} = \psi^6 \tilde{A}_{ij}$  and  $\hat{A}^{ij} = \psi^6 \tilde{A}^{ij}$ , the Hamiltonian and momentum constraint equations are rewritten in the form

$$\Delta \psi = -2\pi E \psi^5 - \frac{1}{8} \hat{A}_{ij} \hat{A}^{ij} \psi^{-7}, \quad (2.36)$$

$$\hat{A}_i^j_{,j} = 8\pi J_i \psi^6. \quad (2.37)$$

After we decompose  $\hat{A}_{ij}$  in the standard manner as

$$\hat{A}_{ij} = W_{i,j} + W_{j,i} - \frac{2}{3}\delta_{ij}\delta^{kl}W_{k,l}, \quad (2.38)$$

we set  $W_i$  as [18,16]

$$W_i = \frac{7}{8}B_i - \frac{1}{8}(\chi_{,i} + B_{k,i}x^k), \quad (2.39)$$

where  $\chi$  and  $B_i$  denote scalar and vector functions. Then, Eq. (2.37) can be decomposed into two simple elliptic type equations

$$\begin{aligned} \Delta B_i &= 8\pi J_i \psi^6, \\ \Delta \chi &= -8\pi J_i x^i \psi^6. \end{aligned} \quad (2.40)$$

Since  $J_i \psi^6 (= \rho_* \hat{u}_i)$  is non-zero only in the strong field region, the solution of the momentum constraint equation is accurately obtained.

In addition to the constraint equations, we solve an elliptic type equation for  $\alpha$  to impose the maximal slice condition initially. In the conformally flat 3D space, the equation is written in the form

$$\Delta(\alpha\psi) = 2\pi\alpha\psi^5(E + 2S_k^k) + \frac{7}{8}\alpha\psi^{-7}\hat{A}_{ij}\hat{A}^{ij}. \quad (2.41)$$

From the initial condition, the total gravitational mass and angular momentum of the system at  $t = 0$  are calculated from

$$(M_g)_0 = \int d^3x \left( E\psi^5 + \frac{1}{16\pi\psi^7}\hat{A}_{ij}\hat{A}^{ij} \right), \quad (2.42)$$

$$J_0 = \int d^3x (xJ_y - yJ_x)\psi^6. \quad (2.43)$$

Note that Eq. (2.25) reduces to Eq. (2.43) in the 3D space in which  $\tilde{\gamma}_{ij} = \delta_{ij}$  and  $K_k^k = 0$ .

#### D. Boundary conditions

In this paper, we assume  $\pi$ -rotation symmetry around the  $z$ -axis as well as a plane symmetry with respect to the  $z = 0$  plane. Hence, we solve equations in a quadrant region  $L \geq x \geq -L$  and  $L \geq y, z \geq 0$  where  $L$  denotes the location of the outer boundaries. We impose the boundary condition in the  $y = 0$  plane such as

$$Q(x, 0, z) = Q(-x, 0, z), \quad (2.44)$$

$$\begin{aligned} Q^A(x, 0, z) &= -Q^A(-x, 0, z), \\ Q_A(x, 0, z) &= -Q_A(-x, 0, z), \end{aligned} \quad (2.45)$$

$$\begin{aligned} Q^z(x, 0, z) &= Q^z(-x, 0, z), \\ Q_z(x, 0, z) &= Q_z(-x, 0, z), \end{aligned} \quad (2.46)$$

$$\begin{aligned} Q_{AB}(x, 0, z) &= Q_{AB}(-x, 0, z), \\ Q_{Az}(x, 0, z) &= -Q_{Az}(-x, 0, z), \end{aligned} \quad (2.47) \quad (2.48)$$

$$Q_{zz}(x, 0, z) = Q_{zz}(-x, 0, z), \quad (2.49)$$

where  $A$  and  $B = x$  or  $y$ , and  $Q, Q^i(Q_i)$ , and  $Q_{ij}$  denote arbitrary scalar, vector and tensor quantities, respectively.

At the outer boundaries, we impose an approximate outgoing boundary condition for  $h_{ij}$  and  $\tilde{A}_{ij}$  [18] as

$$rQ_{ij}(u) = \text{const}, \quad (2.50)$$

where we set  $u = \alpha t - e^{2\phi}r$ . (Even if we simply set  $u = t - r$ , the results do not change significantly.) More explicitly, Eq. (2.50) is rewritten in the form

$$Q_{ij}(t, r) = \left(1 - \frac{\delta r}{r}\right)Q_{ij}(t - \delta t, r - \delta r), \quad (2.51)$$

where  $\delta t$  is a time step, and  $\delta r = \alpha e^{-2\phi}\delta t$ .  $Q_{ij}(t - \delta t, r - \delta r)$  is linearly interpolated from the nearby 8 grid points. We also note that the numerical results are not sensitive to the boundary condition of  $\tilde{A}_{ij}$  and we have not found significant change in the numerical results even when we impose the boundary condition with the radial fall-off as  $O(r^{-3})$ . A possible explanation for this result is that the spatial derivative of  $\tilde{A}_{ij}$ , which appears in the evolution equations for  $\tilde{A}_{ij}$  and  $F_i$ , does not play an important role for evolution of the system. On the other hand, numerical results and stability of the numerical system are significantly dependent of the boundary condition for  $\tilde{\gamma}_{ij}$ . The condition defined by Eq. (2.51) is one of the best conditions among those we have tried so far.

For  $\phi$  and  $K_k^k$ , we impose the following boundary conditions at the outer boundaries

$$(r\phi)_{,r} = 0, \quad (2.52)$$

$$K_k^k = 0. \quad (2.53)$$

For  $F_i$ , we have tried a number of boundary conditions such as  $F_i = O(r^{-3})$ ,  $F_i = 0$ , and  $\partial_j F_i = \text{const}$  at  $x_j = L$ , and have found that the results are weakly dependent of the boundary condition. We have found that the condition  $F_i = 0$  is preferable for a long-timescale numerical evolution, but for extracting gravitational waves near the outer boundaries, the condition  $F_i = O(r^{-3})$  or  $\partial_j F_i = \text{const}$  is preferable. In the spherical cases, we use the condition  $F_i = 0$ , but we change the condition case by case for other cases.

It should be noted that all the outer boundary conditions described above are only approximate. This implies that numerical errors such as spurious back reflection and incoming of gravitational waves will be generated near the outer boundaries. For precise numerical simulation, apparently, we have to adopt more sophisticated outer boundary conditions as have been proposed and investigated by a couple of groups [21]. Imposing precise outer boundary conditions is one of important future issues.

### E. Grid and time step

Throughout this paper, we use a uniform grid, i.e.,  $\delta x = \delta y = \delta z = \text{const}$ . We take  $(2N+1, N+1, N+1)$  grid points in  $(x, y, z)$  direction, respectively (i.e.,  $N = L/\delta x$ ).

The time step  $\delta t$  must satisfy the stability condition restricted by the Courant criterion for geometric variables. If we neglect the other two directions, the geometric Courant condition in the  $x^i$  direction is written as

$$\delta t < [\alpha \gamma_{ii}^{-1/2} + \beta^i]^{-1} \delta x. \quad (2.54)$$

Since  $[\alpha \gamma_{ii}^{-1/2} + \beta^i]^{-1}$  is expected to be greater than unity for most cases, we simply set a geometric time step as

$$\delta t_g = C_g \delta x, \quad (2.55)$$

where  $C_g$  is a constant which we choose typically as 0.3. Also,  $\delta t$  must be sufficiently small so that the matter distribution cannot change by a large fraction amount in one time step. The timescale is shortest when the matter

distribution changes in a dynamical timescale as in the case when the matter collapses to a singularity. Thus, we simply set

$$\delta t = \min(C_m \sqrt{\frac{3\pi}{32\rho_*}}, \delta t_g), \quad (2.56)$$

where  $C_m$  is a constant for which we choose  $0.02 - 0.04$ . Note that the first term in the right-hand side of Eq. (2.56) denotes the time for the collapse to a singularity of a spherical, homogeneous dust in the Newtonian limit.

In the case when the density is so high that a black hole seems to be formed, the first term of Eq. (2.56) is smaller than the second term, but besides such a highly relativistic case, the second term is smaller and determines the time step. We note that the hydrodynamic Courant condition is less severe than the geometric one [22], so that we do not consider it.

### F. Brief summary of numerical methods and evolution scheme

For solving the equations for geometric variables as well as for determining the apparent horizon, the same methods as employed in previous papers [18,16] are used here. The numerical method for solving the hydrodynamic equations is briefly discussed in Appendix A.

The evolution scheme for the geometric and fluid variables from a time slice at  $t$  to the next time slice at  $t + \delta t$  is as follows (see the schematic figure 1): We put  $\tilde{\gamma}_{ij}$ ,  $F_i$ ,  $\phi$ ,  $\alpha$ ,  $\beta^k$ ,  $\rho_*$ ,  $\hat{u}_i$ ,  $v^i$ , and  $e_*$  on  $t^{(0)}, t^{(1)}, \dots, t^{(n)}$  and  $\tilde{A}_{ij}$  and  $K_k^k$  on  $t^{(-1/2)}, t^{(1/2)}, t^{(3/2)}, \dots$ , and  $t^{(n-1/2)}$ , where  $t^{(n)}$  denotes the coordinate time at the  $n$ -th time step,  $t^{(n+1/2)} \equiv (t^{(n)} + t^{(n+1)})/2$ , and  $n$  is a positive integer. Namely, we use the leapfrog method [23] for evolution of the geometric variables.

For a given set of the geometric variables  $\tilde{\gamma}_{ij}$ ,  $F_i$ ,  $\phi$ ,  $\alpha$ ,  $\beta^k$  and fluid variables  $\rho_*$ ,  $\hat{u}_i$ ,  $v^i$ , and  $e_*$  at  $t^{(n)}$ , and other geometric variables  $\tilde{A}_{ij}$  and  $K_k^k$  at  $t^{(n-1/2)}$  (the stage (1) of Fig. 1), first,  $\tilde{A}_{ij}$  and  $K_k^k$  are evolved from  $t^{(n-1/2)}$  to  $t^{(n+1/2)}$  using the evolution equations (2.20) and (2.22) (the stage (2) of Fig. 1). Since the right-hand side of these evolution equations includes  $\tilde{A}_{ij}$  and

$K_k^k$  which are defined only at  $t^{(n-1/2)}$ , we use the linear extrapolation method at each spatial grid point as

$$(K_k^k)^{(n)} = \frac{3}{2}(K_k^k)^{(n-1/2)} - \frac{1}{2}(K_k^k)^{(n-3/2)},$$

$$(\tilde{A}_{ij})^{(n)} = \frac{3}{2}(\tilde{A}_{ij})^{(n-1/2)} - \frac{1}{2}(\tilde{A}_{ij})^{(n-3/2)},$$

to preserve the second order accuracy in time. We note that in adopting the linear extrapolation, we implicitly make use of the fact that the time steps at  $t^{(n-1)}$  and  $t^{(n)}$  are approximately equal.

Once we obtain  $(K_k^k)^{(n+1/2)}$  and  $(\tilde{A}_{ij})^{(n+1/2)}$ , the geometric variables  $\tilde{\gamma}_{ij}$ ,  $\phi$  and  $F_i$  are evolved to  $t^{(n+1)}$  (the stage (3) of Fig. 1). We also use the extrapolation method such as

$$\alpha^{(n+1/2)} = \frac{3}{2}\alpha^{(n)} - \frac{1}{2}\alpha^{(n-1)},$$

$$(\beta^i)^{(n+1/2)} = \frac{3}{2}(\beta^i)^{(n)} - \frac{1}{2}(\beta^i)^{(n-1)},$$

because they are necessary to preserve the second order accuracy in time.

Next, the hydrodynamic equations for  $\rho_*$ ,  $\hat{u}_i$ , and  $e_*$  are evolved to  $t^{(n+1)}$ . For solving the evolution equations, we use a Runge-Kutta method of second order accuracy [23]; i.e., the hydrodynamic equations are solved from  $t^{(n)}$  to  $t^{(n+1/2)}$  in the first step (the stage (4) of Fig. 1), and using the fluid variables defined both at  $t^{(n)}$  and at  $t^{(n+1/2)}$ , those at  $t^{(n+1)}$  are subsequently obtained in the second step (the stage (5) of Fig. 1). Since there appear  $\tilde{\gamma}_{ij}$ ,  $\phi$ ,  $\alpha$ ,  $\beta^i$ ,  $w$ ,  $h$ , and  $P$  in the right-hand side of the relativistic Euler equation (2.10) and we need those at  $t^{(n+1/2)}$  in the second step for solving the equation, we use the extrapolation and interpolation,

$$\alpha^{(n+1/2)} = \frac{3}{2}\alpha^{(n)} - \frac{1}{2}\alpha^{(n-1)},$$

$$(\beta^i)^{(n+1/2)} = \frac{3}{2}(\beta^i)^{(n)} - \frac{1}{2}(\beta^i)^{(n-1)},$$

$$\phi^{(n+1/2)} = \frac{1}{2}[\phi^{(n+1)} + \phi^{(n)}],$$

$$(\tilde{\gamma}_{ij})^{(n+1/2)} = \frac{1}{2}[(\tilde{\gamma}_{ij})^{(n+1)} + (\tilde{\gamma}_{ij})^{(n)}],$$

$$w^{(n+1/2)} = \frac{3}{2}w^{(n)} - \frac{1}{2}w^{(n-1)}.$$

$P$  and  $h$  at  $t^{(n+1/2)}$  are calculated from  $\rho_*$ ,  $e_*$ ,  $w$  and  $\phi$  at  $t^{(n+1/2)}$  obtained in the first step. (Note that  $w^{(n+1)}$ ,

$\alpha^{(n+1)}$  and  $(\beta^i)^{(n+1)}$  have not yet been obtained by this stage.) Once the fluid variables are evolved to  $t^{(n+1)}$ , Eq. (2.14) is solved at each spatial grid point for obtaining  $w^{(n+1)}$  using the Newton-Raphson method [23]. Subsequently, we can obtain  $P$  and  $h$  at  $t^{(n+1)}$ .

In the final step, we determine  $\alpha^{(n+1)}$  and  $(\beta^i)^{(n+1)}$  by imposing the gauge conditions (the stage (6) of Fig. 1). In solving their equations, we again use the extrapolation as

$$(K_k^k)^{(n+1)} = \frac{3}{2}(K_k^k)^{(n+1/2)} - \frac{1}{2}(K_k^k)^{(n-1/2)},$$

$$(\tilde{A}_{ij})^{(n+1)} = \frac{3}{2}(\tilde{A}_{ij})^{(n+1/2)} - \frac{1}{2}(\tilde{A}_{ij})^{(n-1/2)}.$$

Since all the quantities are evolved by this stage, we can derive  $v^i$  at  $t^{(n+1)}$  using Eq. (2.12) without any extrapolation.

### III. TESTS AND RESULTS

Our current priority in numerical relativity is to perform simulations of the merger of binary neutron stars. Before carrying out such simulations successfully, it is necessary to confirm the accuracy and performance of our numerical code for many different problems. In particular, the following issues have to be addressed: (i) the merger will take place for a couple of orbital periods from the time when the binary just enters inside the ISCO to formation of a black hole or neutron star. Can we carry out the simulation stably for a couple of orbital periods ? (ii) the final product of the merger will either be a black hole or a neutron star. If the merged object is unstable against gravitational collapse, a black hole is formed. Can we judge the stability of the merged object against the gravitational collapse ? (iii) the formation of a black hole will be signaled by the appearance of an apparent horizon. Can we determine the apparent horizon during the simulations ? (iv) can we extract waveforms of gravitational waves ?

To answer these questions, we have performed simulations for a wide variety of test problems:

1. Spherical collapse of dust ( $P = 0$ ) to a black hole:

We compare the results with those obtained in a 1D (spherical symmetric) simulation. We also check whether the apparent horizon can be found at a correct time and location. This test confirms that our code can simulate the formation of a black hole accurately.

2. Stability of spherical stars: We check that the stability of spherical stars can be judged in our code preparing both stable and unstable stars as initial conditions. We also check whether our code can provide a correct output on the fundamental radial oscillation frequency of perturbed spherical stars. This test is useful to confirm that we can determine the stability of the merged object against gravitational collapse.

3. Quadrupole oscillations of perturbed spherical stars and emission of gravitational waves: We give a quadrupole perturbation to a spherical stable star, and check whether we can obtain the frequency of the fundamental mode ( $f$ -mode) oscillation and extract the waveform of gravitational waves near the outer boundaries. This test is useful to confirm that the extraction of gravitational waves near the outer boundaries is feasible.

4. Preservation of rapidly rotating stars in equilibrium states: We check that (approximate) equilibrium states of rapidly rotating, stable stars can be preserved for a couple of the rotation periods. The simulations are carried out choosing rigidly and rapidly rotating stars at mass-shedding limits. This test is useful to confirm that the coordinate twisting due to the rotation of the stars is sufficiently suppressed to a level adequate to carry out stable and accurate simulations in our AMD gauge condition.

5. Preservation of a corotating binary neutron star in a quasi-equilibrium state: We prepare a mildly relativistic corotating binary neutron star in an

approximate quasi-equilibrium state obtained assuming a conformally flat 3D geometry [24]. Although we ignore  $h_{ij}$  which is necessary to obtain a true quasi-equilibrium configuration, it is at most a second post Newtonian quantity from the post Newtonian point of view [25] and for mildly relativistic binaries, the error is expected to be small. This test confirms that an approximate quasi-equilibrium state of a binary neutron star can be preserved for more than one orbital period.

In the following subsections, we present the numerical results of the tests 1–5 separately.

In the tests 2–5, we prepare the equilibrium and/or quasi-equilibrium states as the initial conditions adopting a polytropic equation of state  $P = K\rho^\Gamma$  with  $\Gamma = 5/3$  and/or 2. For  $\Gamma = 5/3$  and 2, we fix  $K$  as 10 and  $200/\pi$ , respectively, to mimic a relation between the rest mass  $M_*$  and the central density  $\rho_c$  for neutron stars.

In Fig. 2, we show  $M_*$  and the circumferential radius  $R$  of the spherical equilibrium stars as a function of  $\rho_c$  for  $\Gamma = 5/3$  and 2, respectively. For  $\Gamma = 5/3$ ,  $M_*$  ( $M_g$ ) reaches a maximum value  $\simeq 1.552$  (1.487) at  $\rho_c \simeq 1.85 \times 10^{-3}$ , and for  $\Gamma = 2$ ,  $M_*$  ( $M_g$ )  $\simeq 1.435$  (1.306) at  $\rho_c \simeq 5.0 \times 10^{-3}$ . Beyond the critical densities, the star is unstable.

Although we adopt particular units fixing  $K$ , the mass, length, and density may be rescaled using the following rule

$$M_*(M_g) \rightarrow M_* C^{\bar{n}/2} (M_g C^{\bar{n}/2}), \quad R \rightarrow R C^{\bar{n}/2}, \\ \rho_c \rightarrow \rho_c C^{-\bar{n}} \quad \text{and} \quad J \rightarrow J C^{\bar{n}} \quad \text{for} \quad K \rightarrow K C, \quad (3.1)$$

where  $\bar{n} = 1/(\Gamma - 1)$  and  $C$  is an arbitrary constant. Namely, the invariant quantities are only the dimensionless quantities such as  $M_* K^{-\bar{n}/2}$  ( $M_g K^{-\bar{n}/2}$ ),  $R K^{-\bar{n}/2}$ ,  $\rho_c K^{\bar{n}}$ ,  $M_*/R(M_g/R)$ , and  $J/M_*^2$  ( $J/M_g^2$ ).

### A. Test 1: Spherical collapse of dust

We consider a time symmetric, conformally flat initial condition for the dust sphere, and adopt the following

density profile

$$\rho_* = A \left[ 1 + \exp\left(\frac{r^2 - r_0^2}{\delta r^2}\right) \right]^{-1}, \quad (3.2)$$

where we choose  $r_0 = 4M_g$  and  $\delta r^2 = 0.18M_g^2$ .  $A$  is adjusted so that the gravitational mass of the system is 1 ( $A \simeq 4.287 \times 10^{-3}$ ). In this test, we assign the negligible specific internal energy and pressure, i.e.,  $\varepsilon \ll 1$  and  $P \ll \rho$ . Throughout this subsection, every quantity is shown in the unit  $M_g = 1$  (and  $G = 1 = c$ ).

We perform the 3D numerical simulation as well as 1D (spherical symmetric) simulation and compare two results. The simulations are carried out in two different spatial gauge conditions, the MD and  $\beta^i = 0$  gauge conditions. We note that in a spherical symmetric case with a conformally flat initial condition, the AMD gauge condition is identical with the MD gauge condition because the condition  $\partial_t \tilde{\gamma}_{ij} = 0$  holds in both cases throughout the whole evolution. Hence, the comparison can be done without any coordinate transformation. We use the maximal slice condition in the 1D case and AMS condition in the 3D case. Since  $K_k^k$  can be kept nearly equal to zero in the AMS condition, we can consider them as the same slice conditions. We have used a grid with  $N = 60$  and  $\delta x = 0.15$  in the 3D simulation.

First, we show numerical results for the  $\beta^k = 0$  case. In Fig. 3, we show  $\alpha$  and  $\rho_*$  at  $r = 0$  as a function of time. The dotted and solid lines are the 1D and 3D results, respectively. In Fig. 4, we also plot  $\alpha$  along the  $x$ -axis at selected times ( $t = 12.0, 17.2$  and  $20.4$ ) for the 1D (the solid lines) and 3D (the filled circles) results, respectively. We note that in the 1D simulation, the apparent horizon is found at  $t \sim 18.6$ . In the 3D simulation, it is also found nearly at the equal time and the same location. These results show that the 1D and 3D results agree well at least up to the formation of a black hole and confirm that it is possible to investigate a black hole formation in a spherical symmetric spacetime accurately with our formulation and numerical code.

In the late phase ( $t \gtrsim 23$ ), the accuracy of the 3D results deteriorates. This is because the error increases

in  $\tilde{\gamma}_{ij}$  rapidly as a consequence of the so-called horizon stretching around the location of the apparent horizon.

Next, we present numerical results in the MD (and AMD) gauge conditions. In Fig. 5, we show  $\alpha$  and  $\rho_*$  at  $r = 0$  as a function of time. In this case, the 1D (the dotted lines) and 3D (the solid lines) results agree well by  $t \sim 20$ . Fortunately, we could determine the apparent horizon because it is formed  $t \sim 18.6$ , but the accuracy deteriorates soon after the formation. This illustrates that the MD gauge condition is less appropriate than  $\beta^k = 0$  gauge condition for evolution of the late phase of the gravitational collapse in the simulations performed under identical grid number and spacing. The reason is apparently related to the drawback of the MD gauge conditions pointed out in [16]: In the MD or AMD gauge conditions with  $K_k^k \simeq 0$ , the coordinates spread outward and the proper distance between two neighboring grids increases, i.e.,  $\partial_i \beta^i > 0$  ( $\beta^r > 0$ ) and  $\partial_t \phi > 0$  (cf. Eq. (2.21)), around  $r = 0$  during gravitational collapses. As a result, the black hole forming region cannot be well resolved. In Fig. 6, we show the time evolution of  $\phi$  at  $r = 0$ . It changes from 0.17 to 0.9 by  $t = 20$ . Thus, the proper distance between two neighboring grids increases by a factor  $e^{2(\phi(t=20) - \phi(t=0))} \sim 4$ . In the  $\beta^i = 0$  gauge condition with  $K_k^k = 0$ , on the other hand,  $\phi(x^i)$  is constant in time and  $h_{ij}$  for  $r \sim 0$  is nearly equal to 0, so that the physical grid spacing in the MD gauge conditions is 4 times as large as that in the  $\beta^i = 0$  gauge condition around  $r = 0$  at  $t \sim 20$ .

To overcome the coordinate spreading effect without changing the gauge condition, we have to take a large number of grid points around the black hole forming region. The solution to this problem may be to adopt an adaptive mesh refinement technique [26] in which we can improve the resolution around the black hole forming region effectively. However, since the spreading factor increases rapidly as shown in Fig. 6, we have to improve the resolution also quickly when using such a technique. We do not think it a good idea to simply rely on such a technique. We consider it necessary to modify the gauge

condition. A strategy of the modification and the numerical experiment will be presented in one of forthcoming papers [27].

### B. Test 2: Stability of spherical stars

In this second test, we prepare spherical equilibrium stars of a polytropic equation of state of  $\Gamma = 5/3$ . We use two stars for the test. One is a stable star of  $\rho_c = 10^{-3}$ ,  $M_* = 1.499$ , and  $M_g = 1.440$ , and the other is an unstable star of  $\rho_c = 2.4 \times 10^{-3}$ ,  $M_* = 1.542$ , and  $M_g = 1.478$ . In both cases, the total rest mass is slightly less than the maximum value. In Fig. 2, we show with the filled circles and the open circle the locations of the two stars and the star at the critical density of stability, respectively.

Here, we again use two spatial gauge conditions: AMD gauge and  $\beta^i = 0$  gauge conditions. In Fig. 7, we show the time evolution of the density  $\rho (= \rho_* e^{-6\phi}/w)$  and  $\alpha$  at  $r = 0$  as a function of time for a stable configuration of  $\rho_c = 10^{-3}$ . These simulations were performed with  $N = 50$  and  $\delta x = 0.4$ . The solid and dotted lines are the results in the  $\beta^i = 0$  gauge condition, and the dashed line is in the AMD gauge condition. The dotted line also denotes the result for the case in which we give a perturbation to the equilibrium configuration by reducing  $K$  of 0.5% initially. In other cases, we give the equilibrium state without any changes. These figures clearly illustrate the feasibility of our code to judge the stability of the spherical stable star and to preserve it stably at least in a few oscillation periods irrespective of the gauge conditions.

As shown with the approximate perturbation analysis in appendix B [28], the period of the fundamental radial oscillation is  $\sim 10.5\rho_c^{-1/2}$ . For the pressure depleted case (the dotted line), the oscillation period is clearly recognized in Fig. 7. This shows that the frequency of the fundamental radial oscillation can be computed accurately in our code.

In Fig. 8, we show the time evolution of  $\rho$  and  $\alpha$  at  $r =$

0 for an unstable configuration of  $\rho_c = 2.4 \times 10^{-3}$ . The simulations are performed with  $N = 50$  and  $\delta x = 0.3$ . We prepare pressure depleted initial conditions in which we reduce  $K$  by 0.5% and 0.1%. As in the stable case, we use both the  $\beta^i = 0$  and AMD gauge conditions, and the numerical results are denoted by the solid and dashed lines, respectively. As shown in Fig. 8, the unstable star collapses into a black hole. As one would expect, the star collapses more quickly in the case when the depletion factor of the pressure is larger. These results confirm that our code provides correct results.

The time evolution of  $\rho$  and  $\alpha$  at  $r = 0$  in the two spatial gauge conditions approximately agrees with each other except for the late phase of the gravitational collapse during which the coordinate spreading effect is severe in the AMD (and MD) gauge conditions [29]. The overall agreement (except for the late phase) is an important test of consistency because  $\rho$  and  $\alpha$  at  $r = 0$  are both gauge independent quantities.

### C. Test 3: Quadrupole oscillations of a perturbed spherical star

For the third test, we prepare stable spherical stars in equilibrium states as in test 2. We adopt  $\Gamma = 5/3$  and 2 in this test, and choose the stars in which  $\rho_c = 10^{-3}$  for  $\Gamma = 5/3$  and  $\rho_c = 3 \times 10^{-3}$  for  $\Gamma = 2$ , respectively. For  $\Gamma = 2$  and  $\rho_c = 3 \times 10^{-3}$ , the mass and circumferential radius are 1.25 and 6.99, respectively (see filled circles in Fig. 2). We perform the simulations with  $N = 50$  and  $\delta x = 0.5$  for  $\Gamma = 5/3$  and with  $N = 50$  and  $\delta x = 0.25$  for  $\Gamma = 2$ , respectively. The test is performed in the AMD gauge condition and at the outer boundaries, we set  $F_i = O(r^{-3})$ .

As the source of the initial quadrupole oscillation, we give a velocity perturbation of “+” type

$$u_i(t = 0) = A \sqrt{\frac{M_g}{R^3}} (-x, y, 0), \quad (3.3)$$

or of “ $\times$ ” type

$$u_i(t = 0) = A \sqrt{\frac{M_g}{R^3}} (-y, -x, 0), \quad (3.4)$$

where  $A$  is a constant which is set to be 0.082.

As a result of a time-varying mass quadrupole moment of the star, gravitational waves are emitted. This allows to check the feasibility of the gravitational wave extraction near the outer boundaries. To extract gravitational waveforms, we define [16]

$$h_+ \equiv r(\tilde{\gamma}_{xx} - \tilde{\gamma}_{yy})/2, \quad (3.5)$$

$$h_\times \equiv r\tilde{\gamma}_{xy}, \quad (3.6)$$

along the  $z$ -axis. Since we adopt the AMD gauge condition and prepare initial conditions in which  $F_i = 0$ ,  $h_{ij}$  is approximately transverse and traceless in the wave zone [16]. As a result,  $h_+$  and  $h_\times$  are expected to be appropriate measures of gravitational waves. They are also useful to find the maximum amplitude of gravitational waves because we treat the problems in which the amplitude is maximum along the  $z$ -axis.

In Figs. 9–11, we show a root mean square radius

$$x_{\text{rms}}^i \equiv \left[ \frac{1}{M_*} \int d^3x \rho_*(x^i)^2 \right]^{1/2}, \quad (3.7)$$

as a function of time for the  $+$  and  $\times$  mode perturbations for  $\Gamma = 5/3$  (Figs. 9 and 10), and for  $+$  mode perturbation for  $\Gamma = 2$  (Fig. 11), respectively. In the case of the  $+$  mode oscillation,  $x_{\text{rms}}$  (the solid line) and  $y_{\text{rms}}$  (the dotted line) oscillate with a characteristic period. For  $\Gamma = 5/3$  and 2, the oscillation period is  $\sim 5.5\rho_c^{-1/2}$  and  $\sim 4.7\rho_c^{-1/2}$ , respectively. As shown by perturbative studies on stellar pulsations [30], the angular frequencies of the  $f$ -mode oscillation for  $\Gamma = 5/3$  and 2, and  $M_g/R \sim 0.1$  are approximately written as

$$\omega \simeq \begin{cases} 1.44\sqrt{\frac{M_g}{R^3}} & \text{for } \Gamma = 5/3, \\ 1.22\sqrt{\frac{M_g}{R^3}} & \text{for } \Gamma = 2. \end{cases} \quad (3.8)$$

Or, according to an empirical formula [31], the angular frequency for the stars of  $M_g/R \sim 0.1$  is also written, irrespective of  $\Gamma$ , as

$$\omega \simeq 0.012 + 0.93\sqrt{\frac{M_g}{R^3}}. \quad (3.9)$$

For  $\Gamma = 5/3$  and  $\rho_c = 10^{-3}$  (i.e.,  $M_g \simeq 1.44$  and  $R \simeq 13.1$ ), the oscillation period is  $\simeq 5.5\rho_c^{-1/2}$  in both formulas. For  $\Gamma = 2$  and  $\rho_c = 3 \times 10^{-3}$  (i.e.,  $M_g \simeq 1.25$  and  $R = 6.99$ ), the period is  $\simeq 4.7\rho_c^{-1/2}$  from Eq. (3.8) and  $\simeq 5.0\rho_c^{-1/2}$  from Eq. (3.9). Thus, our numerical results agree with these perturbative results fairly accurately.

On the other hand, the oscillation periods of  $z_{\text{rms}}$  (the dashed line) for the  $+$  mode perturbation and of all the components of  $x_{\text{rms}}^i$  for the  $\times$  mode perturbation are roughly  $\sim 10\rho_c^{-1/2}$  for  $\Gamma = 5/3$  and  $\sim 7\rho_c^{-1/2}$  for  $\Gamma = 2$ . These are in agreement with the periods of the fundamental radial oscillation and different from those of the  $f$ -mode oscillation. This reflects the fact that they are not relevant for the  $f$ -mode oscillation at linear order.

In Figs. 12 and 13, we show  $h_+$  and  $h_\times$  at  $z_{\text{obs}} = 24.5$  (the solid lines) and 19.5 (the dashed lines) for  $\Gamma = 5/3$  as a function of the retarded time for the  $+$  and  $\times$  mode perturbations. In Fig. 14, we also show  $h_+$  and  $h_\times$  at  $z_{\text{obs}} = 12.25$  (the solid lines) and 9.75 (the dashed lines) for  $\Gamma = 2$  for the  $+$  mode perturbation. As the oscillation frequency of the  $f$ -mode shows, the wavelength of gravitational waves is several times larger than  $z_{\text{obs}}$ , so that we expect the extracted waveforms to be different from the asymptotic waveforms. However, they appear to constitute a fair description of the asymptotic waveforms, at worst qualitatively, because (a) the solid and dashed lines approximately agree, i.e.,  $\tilde{\gamma}_{xx} - \tilde{\gamma}_{yy}$  and  $\tilde{\gamma}_{xy}$  behave approximately as  $f(t-z)/z$  along the  $z$ -axis where  $f$  denotes a generic function, (b) the oscillation period agrees well with that of the  $f$ -mode, (c) the order of magnitude of  $h_+$  and  $h_\times$  roughly agrees with that derived by the quadrupole formula, i.e.,  $M_g v^2 \sim M_g^2 A^2 / R \sim 10^{-3}$ , and (d) for the perturbation given by Eq. (3.3),  $h_\times$  remains nearly zero, and for Eq. (3.4),  $h_+$  remains nearly zero, as expected by the quadrupole formula. These facts suggest that  $h_+$  and  $h_\times$  represent (at least approximately) gravitational waves emitted by the stellar oscillation and indicate the ability of our code to extract gravitational waves near the outer boundary. We expect that a simula-

tion of higher resolution would produce even more precise gravitational waveforms.

#### D. Test 4: Stability of rapidly rotating stars

To carry out this test, we prepare rapidly and rigidly rotating neutron stars in (approximate) equilibrium states. We adopt  $\Gamma = 5/3$  and 2, and select stable compact neutron stars.

To prepare the rotating stars in approximate equilibrium states, we use a conformal flatness approximation. Then, the geometric and hydrostatic equations for solutions of equilibrium states are described as [24]

$$\Delta\psi = -2\pi(\rho h w^2 - P)\psi^5 - \frac{\psi^5}{8}\delta^{ik}\delta^{jl}L_{ij}L_{kl}, \quad (3.10)$$

$$\begin{aligned} \Delta(\alpha\psi) = 2\pi\alpha\psi^5[\rho h(3w^2 - 2) + 5P] \\ + \frac{7\alpha\psi^5}{8}\delta^{ik}\delta^{jl}L_{ij}L_{kl}, \end{aligned} \quad (3.11)$$

$$\begin{aligned} \delta_{ij}\Delta\beta^i + \frac{1}{3}\beta^k_{,kj} - 2L_{jk}\delta^{ki}\left(\partial_i\alpha - \frac{6\alpha}{\psi}\partial_i\psi\right) \\ = 16\pi\alpha\rho h w u_j, \end{aligned} \quad (3.12)$$

$$\frac{\alpha h}{w} = \text{const.}, \quad (3.13)$$

where

$$u_i = w\psi^4(\epsilon_{izk}\Omega x^k + \delta_{ij}\beta^j)/\alpha, \quad (3.14)$$

$$w^2 = 1 + \psi^{-4}\delta^{ij}u_iu_j, \quad (3.15)$$

$$h = 1 + K\Gamma\rho^{\Gamma-1}/(\Gamma-1), \quad (3.16)$$

$$L_{ij} = \frac{1}{2\alpha}\left(\delta_{jk}\partial_i\beta^k + \delta_{ik}\partial_j\beta^k - \frac{2}{3}\delta_{ij}\partial_k\beta^k\right), \quad (3.17)$$

and  $\Omega$  denotes the angular velocity of the rotation.

Although the solutions obtained from Eqs. (3.10)–(3.13) are not exact, we can still expect that they are excellent approximate solutions as illustrated in [32]. As shown in Fig. 15, this is the case: We show the gravitational mass  $M_g$  as a function of the central density  $\rho_c$  for rotating stars at mass-shedding limits obtained from exact equations (the solid lines) [33] and obtained by the conformal flatness approximation (the circles). We have found that the sequences of the circles almost coincide with the solid lines for mildly relativistic stars of  $\rho_c \lesssim \rho_t$  where  $\rho_t \sim 0.0015$  for  $\Gamma = 5/3$  and  $\rho_t \sim 0.003$  for

$\Gamma = 2$ . As the density of the rotating stars increases (i.e.,  $\rho_c \gtrsim \rho_t$ ), the coincidence becomes worse gradually, but even for  $\rho_c \sim 2\rho_t$  at which the star seems to be unstable, the difference between the sequences of circles and solid lines is small.

We perform the simulations for the rotating stars marked with the filled circles in Fig. 15. The relevant quantities for the rotating stars are shown in Table I. We adopt  $\delta x = 0.434$  for  $\Gamma = 5/3$  and  $\delta x = 0.202$  for  $\Gamma = 2$  as the grid spacing. With these grid spacings, the major and minor axes of the stars are initially covered by 40 and  $23 - 24$  grid points, respectively.

To suppress the coordinate twisting, the AMD gauge condition is adopted. The shift vector  $\beta^k$  determined in this gauge condition for the conformal 3D metric ( $\tilde{\gamma}_{ij} = \delta_{ij}$ ) agrees with that obtained from Eq. (3.12). This implies that when a simulation is started, the gauge condition is identical with that used for obtaining the approximate equilibrium states. Therefore, we can use the approximate equilibrium states as the initial conditions without any coordinate transformation.

In this test,  $F_i$  is set to be zero at the outer boundaries. The grid number  $N$  is set to be 54 typically. We also adopted  $N = 76$  without changing the grid spacing in some of the following simulations, but we did not find significant difference in the results. This indicates that the outer boundary condition adopted here is adequate.

We have considered two kinds of initial conditions: In one case, we use the approximate equilibrium configurations without any change. In the other case, we initially decrease the pressure by reducing  $K$  of 1% (i.e.,  $\Delta K/K = 1\%$ ). Even in the pressure depleted case, the stars should be stable because the gravitational mass is  $\sim 3 - 5\%$  smaller than the maximum mass of the rotating stars (see Fig. 15). In Fig. 16, we show snapshots of the density contours lines for  $\rho_*$  and the velocity field for  $(v^x, v^y)$  in the equatorial plane (left) and in the  $y = 0$  plane (right) at selected times for  $\Delta K = 0$  and for  $\Gamma = 2$  as an example (for  $\Gamma = 5/3$ , we have found that similar figures can be drawn). We also show  $\alpha$  and  $\rho$  at  $r = 0$  as

a function of  $t/P$  in Fig. 17,  $x_{\text{rms}}$  and  $z_{\text{rms}}$  as a function of  $t/P$  in Fig. 18, and  $J/J_0$  as a function of  $t/P$  in Fig. 19 for  $\Delta K = 0$  (the solid lines) and  $\Delta K/K = 1\%$  (the dotted lines) and for  $\Gamma = 5/3$  and 2. Because of numerical dissipation at the stellar surface, the total angular momentum of the system ( $J$  in Eq. (2.25)) decreases by  $\sim 2\%$  by  $t \sim 2P$  in all the simulations (see Fig. 19). As a result,  $\alpha$  at  $r = 0$  and  $x_{\text{rms}}^i$  decrease and  $\rho$  at  $r = 0$  increases with the time evolution. Also, the stars suffer slight non-axisymmetric (quadrangular shape) deformation near the surface (see Fig. 16) because we use the Cartesian coordinates for rotating stars of a spheroidal shape. However, besides these slight changes, the stars remain almost in the stationary states for more than two rotational periods (i.e., by the time when we terminated these simulations).

Since the initial conditions adopted are only approximate equilibrium states, some oscillations are induced with time evolution. However, the amplitude is very small and cannot be distinguished from the numerical errors. Thus, the states of the rotating stars are close to the true equilibrium ones. Actually, the absolute value of each component of  $h_{ij}$  remains small and of order  $\sim 0.05$ . These results re-confirm that the conformal flatness approximation is really a good approximation for obtaining axisymmetric rotating stars in equilibrium states.

For  $\Delta K/K = 1\%$ ,  $\alpha$  and  $\rho$  at  $r = 0$  and  $x_{\text{rms}}^i$  oscillate with the time evolution. The oscillation period is roughly  $0.9P$  for both  $\Gamma = 5/3$  and 2. We deduce that the period denotes a fundamental quasi-radial oscillation period of the rotating stars.

We emphasize that the simulations can be stably carried out for more than two orbital periods without any instabilities and with  $h_{ij}$  being kept small. These results clearly demonstrate that our formulation for solving the Einstein equation is robust even for systems of non-zero angular momentum and that the coordinate twisting is sufficiently suppressed to a level adequate for long-timescale simulations in our AMD gauge condition.

In this paper, we only perform test simulations us-

ing stable rotating stars. It is very interesting to perform simulations adopting rapidly rotating supramassive neutron stars to investigate the stability and the fate of unstable stars [38]. Such rapidly rotating supramassive neutron stars may be frequently formed as a result of accretion onto a neutron star from a companion star in normal binary systems [39]. However, such simulations are beyond the scope of this paper. More detailed analysis of the stability of rapidly rotating stars and of the final fate of unstable stars will be presented in [27].

#### E. Test 5: Corotating binary in an approximate quasi-equilibrium state

In the final test, we adopt a mildly relativistic corotating binary neutron star in an approximate quasi-equilibrium state as initial condition. As mentioned in Sec. I, our purpose in future is to carry out simulations of coalescing binary neutron stars from the ISCO to formation of a black hole or new neutron star. In the early stage in which the binary is near the ISCO, the radial velocity of each star is expected to be small, and we can consider the binaries as on approximate quasi-equilibrium orbits rather than on plunging orbits. As the radial velocity gradually increases, the orbit changes from the near inspiraling one to the plunging one. For a successful simulation of a coalescing binary neutron star, therefore, the nearly quasi-equilibrium orbit has to be maintained at least for  $\sim 1$  orbital period stably. In this test, we show this feasible with our code.

The configuration of a binary neutron star is again obtained in the assumption of the conformally flat 3D metric and the maximal slice condition  $K_k^k = 0$  [24]. We prepare a binary in which the surfaces of two stars come into contact. We adopt  $\Gamma = 5/3$  in this test. The equation of state for such small  $\Gamma \lesssim 2$  is not so stiff that binary neutron stars in contact orbits are stable against a hydrodynamic instability [24]. Since the binary neutron star is not very compact (see Table II) and is also far from the ISCO, it can remain on the stable orbit for a time comparable with the emission timescale of gravitational

waves.

Approximate quasi-equilibrium states of binary neutron stars are obtained solving Eqs. (3.10–3.13). The equations are solved using a numerical method similar to that employed in [34].

In Fig. 2, we denote, by the cross (of higher density,  $\rho_{\max} = 10^{-3}$ ), the relation between the maximum density  $\rho_{\max}$  and half of the total rest mass  $M_*/2$  for the corotating binary neutron star in an approximate quasi-equilibrium state which is used as an initial condition of the simulation. We compared the numerical results on the relation between the maximum density and rest mass with those by Baumgarte et al. [24], and found that they agree within 2% error. In Table II, we also list the relevant quantities of the binary neutron star. We define an orbital radius  $a \equiv M_g^{1/3} \Omega^{-2/3}$ , and we define an approximate ratio of the emission timescale of gravitational waves to the orbital period as

$$R_\tau = \frac{5}{128\pi} \left( \frac{a}{M_g} \right)^{5/2} = \frac{5}{128\pi} (M_g \Omega)^{-5/3}, \quad (3.18)$$

where we have used the Newtonian expression of the energy and orbital period, and the quadrupole formula for the energy luminosity of gravitational waves [37]. Since our purpose is to check the feasibility of our code to preserve the approximate quasi-equilibrium state stably, this test should be performed for a binary in which  $R_\tau > 1$ .

In the numerical simulation, we adopt the AMD gauge condition to sufficiently suppress the coordinate twisting. As we discussed in Sec. III.D, the gauge condition at  $t = 0$  is identical with that used for obtaining the approximate quasi-equilibrium state, so that we do not have to carry out coordinate transformation at  $t = 0$ .

In this subsection, we adopt the grid spacing as  $\delta x = 0.927$ , varying the grid number  $N$  as 76 and 116. With this setup, the major diameter of each star is covered by 30 grid points initially. For  $N = 76$  and 116,  $L (= N\delta x)$  is only  $\sim 0.2$  and 0.3 times as large as the wavelength of gravitational waves  $\lambda_{\text{gw}} \equiv \pi/\Omega$ . For a precise simulation, the outer boundary should be located in the wave zone so that  $L \gg \lambda_{\text{gw}}$ . This is because we should impose an

outgoing boundary condition for  $\tilde{\gamma}_{ij}$  and  $\tilde{A}_{ij}$ , and in the system of binary neutron stars, the existence of gravitational waves plays an important role for evolution of the system. We have found that the present incomplete treatment for the outgoing boundary conditions seems to produce numerical errors (see below further discussion). However, for imposing the boundary condition in the wave zone with the uniform grid, it is necessary to take a very large grid number  $N \geq 400$ . That is not feasible in the present computational resources on supercomputers. In this paper, we perform simulations overlooking the deficits. Thus, the radiation reaction of gravitational waves is not precisely taken into account in the following simulation. A large simulation of  $L > \lambda_{\text{gw}}$  is one of future issues.

In Fig. 20, we show snapshots of the density contour lines for  $\rho_*$  and velocity field for  $(v^x, v^y)$  in the equatorial plane at selected times for  $N = 116$  while in Fig. 21, we show  $x_{\text{rms}}^i$  as a function of  $t/P$ . We note that if the binary remains in a quasi-equilibrium state, the orbital period should be kept to  $\sim P$ , the curves for  $x_{\text{rms}}$  and  $y_{\text{rms}}$  should be complete sine curves, and  $z_{\text{rms}}$  should be a constant. From Figs. 20 and 21, it is evident that the state of binary neutron star fluctuates from the initial state with time. The fluctuations seem to be mainly due to the numerical error discussed below. Besides the spurious numerical effect, the binary neutron star is kept in an approximate quasi-equilibrium circular orbit for  $\gtrsim 1$  orbital periods stably.

There appear to be two candidates for the numerical error. One is the numerical dissipation of the angular momentum at the stellar surface [35] which was already pointed out in test 4. This is a simple consequence of insufficient resolution. As a result, the orbital radius decreases. The other candidate is the incomplete treatment of the outgoing boundary conditions. As mentioned before, we impose an approximate outgoing boundary condition for  $\tilde{\gamma}_{ij}$  and  $\tilde{A}_{ij}$  not in the wave zone. From this incomplete treatment, the angular momentum seems to go out and come in inaccurately from the outer bound-

aries. As a result, the orbital radius increases and decreases. To illustrate the fact,  $J/J_0$  as a function of  $t/P$  is depicted in Fig. 22. From this figure, we can recognize that the angular momentum increases and decreases with time by  $\sim \pm 3\%$  of the total angular momentum. We note that the angular momentum should be monotonically dissipated by gravitational radiation by about 2% of the total angular momentum in one orbital period according to the estimation by the quadrupole formula. However, the numerical results do not reflect this effect accurately.

Despite these errors, however, the binary neutron star is preserved in the approximate quasi-equilibrium orbit for more than one orbital periods *stably*. This seems to imply that we are choosing an adequate gauge condition and formulation of the Einstein equation. We therefore expect that if we could perform a simulation taking a sufficient number of grid points to impose the outer boundary conditions in the wave zone and to improve the resolution, it would be possible to perform the simulation not only stably, but also accurately.

During the evolution,  $h_{ij}$  deviates from zero and gradually reaches a finite amplitude. The maximum absolute value of each component is of order  $\sim 0.05$  by  $\sim P$ . (This is roughly consistent with what is inferred from a post Newtonian study [25] in which  $h_{ij}$  has magnitude of order  $\sim (M_g/a)^2$ .) Since  $h_{ij}$  becomes non-zero, it could slightly affect the quasi-equilibrium configuration of binary neutron stars. However, this does not seem to be a serious perturbation for the present mildly relativistic case.

In Fig. 23, we show  $h_+$  and  $h_\times$  as a function of  $t/P$ . The solid and dotted lines are extracted at  $z_{\text{obs}} = 106.6$  and 85.3 for  $N = 116$ , and the dashed line at  $z_{\text{obs}} = 69.5$  for  $N = 76$ . As mentioned before, we extract them at  $\sim 0.2 - 0.3\lambda_{\text{gw}}$ , so that they only indicate approximate asymptotic waveforms. Nevertheless, we find that they behave in the periodic manner and that the period approximately agrees with the orbital period. Furthermore, the solid and dotted lines agree very well, implying that

the waves propagate at the speed of light. These facts indicate that the approximate waveforms constitute a fair description of the asymptotic ones.

There are, however, differences from what is expected in the asymptotic waveforms. The first one is found in the long wavelength modulation (apparent especially in  $h_+$ ), which should not appear in the correct waveforms. The modulation is larger for the simulation with smaller  $N$ , indicating that it is caused in the outer boundaries. The second difference is found in the irregular, non-periodic waveforms in the early stage for  $t \lesssim z_{\text{obs}}$ . These waves are emitted because we set an approximate quasi-equilibrium state as the initial condition neglecting  $h_{ij}$ . The first radiation will be the relaxation of the system to the true quasi-equilibrium state. To avoid this shortcoming, we have to prepare more realistic quasi-equilibrium states adopting a formalism in which  $h_{ij}$  is appropriately taken into account. The third difference is found in the amplitude: For the case where two point particles of equal mass are in a circular orbit, the maximum amplitudes of  $h_+$  and  $h_\times$  in the post Newtonian approximation can be written as [36]

$$M_g \tilde{x} \left[ 1 - \frac{17}{8} \tilde{x} + 2\pi \tilde{x}^{3/2} - \frac{15917}{2880} \tilde{x}^2 \right] \quad (3.19)$$

where  $\tilde{x} = (M_g \Omega)^{2/3}$ . Using this formula, the maximum value of  $h_+$  and  $h_\times$  in the binary of  $M_g = 2.92$  and  $\tilde{x} = 0.0887$  is 0.24. (Note that in the quadrupole formula, it is 0.26.) Since the convergence of the post Newtonian formula for  $\tilde{x} \sim 0.1$  is not very good, we should take into account an error of  $\sim 10\%$ . Even if we consider such error, the amplitude obtained in the numerical simulation is found to be somewhat smaller than that derived from Eq. (3.19). The reason seems again due to the incomplete treatment of the outgoing boundary condition at  $L \sim 0.2 - 0.3\lambda_{\text{gw}}$ .

In summary, we can perform simulations of corotating binary neutron stars in an approximate quasi-equilibrium state stably and fairly accurately, and extract gravitational waves with  $\sim 10\%$  error even in the present restricted grid numbers. However, to improve the accuracy

for gravitational waveforms, it is necessary to adopt more sophisticated boundary conditions [21], to take a larger number of grid points and to prepare a more realistic quasi-equilibrium state as the initial condition. These issues will be addressed in future simulations.

#### IV. MERGER OF COROTATING BINARY NEUTRON STARS: A DEMONSTRATION

In this section, we show numerical results of merger between two neutron stars as demonstration that such simulations are feasible. We again adopt corotating binary neutron stars of  $\Gamma = 5/3$  in contact and in approximate quasi-equilibrium orbits. Two binaries shown in Table II (or in Fig. 2 with crosses) are prepared as the initial conditions: One is the same as that adopted in Sec. III.E, and the other is less relativistic one in which the initial maximum density of each star is  $6 \times 10^{-4}$ . To accelerate the merger, we artificially reduce the angular momentum by 5% in the initial stage; i.e., we reduce the initial values of  $u_x$  and  $u_y$  by 5% uniformly. In this section, we adopt  $N = 116$ .

In Figs. 24 and 25, we show snapshots of the density contours lines for  $\rho_*$  and the velocity field for  $(v^x, v^y)$  in the equatorial plane for  $\rho_{\max}(t = 0) = 10^{-3}$  and  $6 \times 10^{-4}$ , respectively. Since we artificially reduce the angular momentum of the system at  $t = 0$ , the neutron stars approach each other to merge soon after the simulations start. For both types of initial data at  $t \gtrsim 0.5P$  ( $P$  denotes the orbital period of the quasi-equilibrium states without the angular momentum depletion), the neutron stars begin to merge forming spiral arms, and by  $t \sim 1.5P$ , new neutron stars which are nearly axisymmetric are formed. In Figs. 26 and 29, we show snapshots of the density contour lines for  $\rho_*$  in the  $y = 0$  plane at  $t = 1.62P$  for  $\rho_{\max}(t = 0) = 10^{-3}$ , and at  $t = 1.59P$  for  $\rho_{\max}(t = 0) = 6 \times 10^{-4}$ . In Fig. 28, we also show the angular velocity  $\Omega \equiv (xv^y - yv^x)/(x^2 + y^2)$  along the  $x$  and  $y$ -axes in the equatorial plane at  $t = 1.62P$  for  $\rho_{\max}(t = 0) = 10^{-3}$  and at  $t = 1.59P$  for  $\rho_{\max}(t = 0) = 6 \times 10^{-4}$ , respectively. These results show that the final

products are rapidly and *differentially* rotating, highly flattened neutron stars. For the case  $\rho_{\max}(t = 0) = 10^{-3}$ , the central density of the merged object for  $t \simeq 1.6P$  is  $\sim 1.4 \times 10^{-3}$ , which is nearly the maximum allowed density along the sequence of stable neutron stars of  $K = 10$  and  $\Gamma = 5/3$  (cf. Figs. 2 and 15). This indicates that the new neutron star is expected to be located near the critical point of stability against gravitational collapse and that a black hole could be formed in the merger of more massive neutron stars.

In Fig. 29, we show fraction of the rest mass inside a coordinate radius defined as

$$\frac{M_*(r)}{M_*} \equiv \frac{1}{M_*} \int_{|x^i| < r} \rho_* d^3x \quad (4.1)$$

as a function of time for  $\rho_{\max}(t = 0) = 10^{-3}$  (the solid lines) and  $\rho_{\max}(t = 0) = 6 \times 10^{-4}$  (the dashed lines). The figures show that  $\simeq 96\%$  and  $\simeq 97\%$  of the matter are inside  $r = 18 (\simeq 6M_g)$  for  $\rho_{\max}(t = 0) = 10^{-3}$  and  $r = 20.4 (\simeq 7.5M_g)$  for  $\rho_{\max}(t = 0) = 6 \times 10^{-4}$  forming the new neutron stars. Thus, only a small fraction of the matter can spread outward to form a halo around the central objects. We also find that  $J(r = 18) \sim 0.85J_0$  for  $\rho_{\max}(t = 0) = 10^{-3}$  and  $J(r = 24.4 = 9M_g) \sim 0.85J_0$  for  $\rho_{\max}(t = 0) = 6 \times 10^{-4}$ . In both cases,  $J/M_g^2$  of the newly formed neutron stars seems roughly  $\sim 1$ , and that appears to be one of the reasons for which the neutron stars do not collapse to be a black hole.

In Fig. 30, we show  $h_+$  and  $h_\times$  as a function of  $t/P$  for the two cases. For  $\rho_{\max}(t = 0) = 10^{-3}$  and  $6 \times 10^{-4}$ ,  $z_{\text{obs}} \simeq 106.6$  and  $126.2$ , respectively. In both cases,  $z_{\text{obs}} \simeq 0.3\lambda_{\text{gw}}$ . In the early phase, their amplitudes gradually increase as their orbital radii decrease. The amplitudes reach their maxima when the neutron stars merge. Since the binaries change their configuration to nearly axisymmetric ones soon after the mergers, the amplitudes drop quickly, leaving quasi-periodic waves of small amplitude which result from small non-axisymmetric perturbations. Since the equation of state is not stiff enough to allow for the bar-mode instability to set in [40], the amplitudes will monotonically fall

in the emission timescale of gravitational waves. For  $\rho_{\max}(t = 0) = 10^{-3}$ , the amplitude rises and falls more sharply than for  $\rho_{\max}(t = 0) = 6 \times 10^{-4}$ , because a higher density merged object is formed more rapidly due to the stronger relativistic gravity. However, the overall waveforms of the two cases closely resemble each other and no significant difference is found besides the difference of their amplitude and frequency. This indicates that the waveforms only weakly depends on the compaction of original neutron stars if black holes are not formed after the merger.

It is interesting to consider the evolution after the formation of a newly formed, differentially rotating massive neutron star of  $J/M_g^2 \sim 1$  such as those obtained in the above simulations. Since the mass of such neutron stars ( $M_g \sim 2.5 - 3M_{\odot}$ ) is much larger than the maximum allowed mass of the original neutron stars of zero angular momentum ( $M_g \sim 1.5M_{\odot}$ ), the new star is strongly supported by the rapid rotation. Hence, if the angular momentum is slightly dissipated or transported outward, they could collapse to be black holes eventually. As discussed in [41], there are many processes which contribute to the angular momentum dissipation and the angular momentum redistribution; e.g., neutrino emission, magnetic radiation, viscous dissipation, and gravitational radiation. Since each process can affect others in complicated manner, it is difficult to give a precise analysis. Here, we present a rough and conservative upper limit of the timescale for collapse to be a black hole.

Since it will be cooled mainly by the neutrino emission [41], the new neutron star will first contract on a neutrino emission timescale  $\tau_{\nu} \sim 10 - 100$  sec after the formation. According to [41], however, the contraction will not lead to a black hole because  $J/M_g^2$  will remain  $\sim 1$  even after a large amount of neutrino emission [41]. Moreover, even in the case  $J/M_g^2 < 1$ , the maximum allowed mass of neutron stars after the cooling may not change significantly if a realistic equation of state is taken into account [42]. The bulk viscosity could play a dominant role when the merged object has high temperature [43] and

high non-axisymmetry. Although the temperature could be sufficiently high just after its formation, the merged object seems to remain nearly axisymmetric during the early stage as suggested by the simulations in this paper. Therefore, the neutron star could not collapse in  $\tau_{\nu}$ .

Nevertheless, the newly formed neutron star is only in a quasi-equilibrium state and is continuously driven away from the equilibrium state. As a result, the neutron star will eventually collapse to a black hole either because of magnetic fields or because of viscosity. An important role in fact could be played by magnetic fields if the neutron stars before the merger had magnetic fields of  $\sim 10^{12}$  Gauss. It seems likely that the strength of magnetic fields of the newly formed neutron star could become larger than their initial strength  $\gtrsim 10^{13}$  Gauss due to the compression of matter during the merger and/or its differential rotation [10]. The angular momentum of the merged object could then be dissipated by the magnetic dipole radiation rather efficiently. The dissipation timescale of the angular momentum is estimated as [44]

$$\tau_B \sim \frac{M_g c^3}{B^2 R^4 \Omega^2} \sim 2 \times 10^7 \text{ sec} \left( \frac{M_g}{3M_{\odot}} \right) \left( \frac{10^{13} \text{ Gauss}}{B} \right)^2 \times \left( \frac{10^6 \text{ cm}}{R} \right)^2 \left( \frac{0.3c}{R\Omega} \right)^2, \quad (4.2)$$

where  $B$  denotes the typical strength of the magnetic field. Thus, the newly formed neutron star could collapse to a black hole within a year if  $B$  is larger than  $10^{13}$  gauss.

If the magnetic field is not very large, on the other hand, the dissipation by the shear viscosity may play a dominant role for evolution of the newly formed neutron star. If the shear viscosity is present, the differential rotation is forced into rigid rotation in viscous timescale. In this case, the angular momentum around the central region is transported to the outer parts and the centrifugal force around the central region is weakened. Because it has a very large mass which is probably the nearly maximum allowed mass for the differential rotation law, the neutron star might collapse as a result of the outward transport of the angular momentum. If the microscopic viscosity is dominant, the dissipation timescale can be estimated as

$$\tau_v \sim \frac{M_g}{\eta_s R} \sim 3 \times 10^8 \text{ sec} \left( \frac{M_g}{3M_\odot} \right) \left( \frac{10^{15} \text{ g/cm}^3}{\rho_c} \right)^{9/4} \times \left( \frac{T}{10^8 \text{ K}} \right)^2 \left( \frac{10^6 \text{ cm}}{R} \right). \quad (4.3)$$

where we use  $\eta_s = 347\rho^{9/4}T^{-2}$  [43] as the shear viscosity of neutron star matter, and  $T$  denotes the temperature which could be dropped by neutrino emission from  $10^{11}\text{K}$  to  $10^{8-9}\text{K}$  in  $\sim 1$  year [45]. It should be noted that even if the magnitude of magnetic fields is not very large, they could be at the origin of an effective viscosity. This is because the differential rotation of the star could cause a shearing instability resulting in the change of the magnetic field configuration and outward transport of the angular momentum [46]. The effective viscous timescale, thus, might be much shorter than that of Eq. (4.3).

We also have to consider the effect of gravitational wave emission due to the bar-mode [40,41] or r-mode [47], by which the non-axisymmetric perturbation may grow contributing the dissipation of the angular momentum or the redistribution of the differential rotation. Such effects are likely to be important, in particular after the newly formed neutron star contracts due to the neutrino emission, because in such stage the ratio of the rotational kinetic energy to the binding energy could become large ( $\gtrsim 0.14$ ) due to the contraction [41] and/or the equation of state could be stiff ( $\Gamma \gtrsim 1.8$  [40]) enough to allow for the bar-mode deformations. Since there are too many uncertain aspects such as the initial amplitude of the non-axisymmetric perturbation and interaction with viscosity [48], the dissipation timescales cannot be estimated in a simple manner. However, it is likely that such effects contribute to the dissipation of the angular momentum and make the timescale shorter. We can then conclude that the newly formed supramassive neutron star (if it could be formed) will eventually collapse to a black hole in the timescale  $\sim 10^{\pm 1}$  years as a result of one of the above dissipation processes.

The argument presented here suggests that the strength of the magnetic field of the newly formed neutron star is one of key parameters for the evolution. It

may well be important to investigate the evolution of the magnetic field during the merger incorporating a solver of the magnetic field equation.

## V. SUMMARY

In this paper, we present our first successful results of numerical simulations carried out using fully general relativistic 3D hydrodynamic code. We have performed a wide variety of simulations for test problems toward more realistic simulations of coalescing binary neutron stars and have confirmed it possible to obtain the solutions for the test problems fairly accurately. In particular, we have illustrated that it is possible to preserve an approximate quasi-equilibrium state of a mildly relativistic binary neutron star as well as to perform simulations of merger between two corotating neutron stars to be new neutron stars stably for a couple of orbital periods in our numerical code. These results indicate that numerical simulations of binary neutron stars for a long time from their ISCO to mergers are feasible.

Since we could not take a sufficiently large number of grid points to impose the outer boundaries in the wave zone as well as to resolve each neutron stars precisely, numerical errors are unavoidably included in the results. In particular, we feel that radiation reaction effect due to gravitational wave emission could not be taken into account precisely. For a more accurate computation of the radiation reaction effect, we will have to adopt a numerical technique such as a nested grid technique which effectively makes the computational region bigger or to impose sophisticated boundary conditions at the outer boundaries [21], unless computational power is improved soon. These issues should be pursued in future works. We emphasize, however, that besides the error induced by the incomplete treatment of the outgoing boundary conditions as well as the numerical dissipation due to the restricted resolution, the simulation can be performed stably and fairly accurately. If we can accept such small error (for example, say  $\lesssim 5\%$  error in the angular mo-

mentum), the code can be used for investigation of many interesting problems even at present.

In this paper, we have paid attention only to test problems. Since we consider binary neutron stars of mildly large compaction parameter and small  $\Gamma$ , the final products of the merger are not black holes. A black hole may be more easily formed for larger  $\Gamma$  and preliminary simulations indicate that this is the case. One of the most interesting and important issues in numerical relativity is to clarify the criterion for formation of black holes. In a forthcoming paper [49], we will perform simulations of corotating binary neutron stars of a large  $\Gamma \sim 2$ , in which a black hole could be formed more easily.

It is well known, however, that the corotating velocity field is not realistic for binary neutron stars because the viscosity of the neutron stars is not large enough to achieve the corotation [50]. Instead, the irrotational velocity field is considered to be more realistic one [50]. For making a realistic model of the final phase of binary neutron stars, it is necessary to perform simulations for irrotational binary neutron stars.

Fortunately, several groups have just recently developed numerical methods for obtaining an approximate quasi-equilibrium state of irrotational binary neutron stars in a conformal flatness approximation [7–9], providing more realistic models of binary neutron stars. Namely, an initial condition has already been prepared. In the next step [49], we will also carry out simulations adopting the approximate quasi-equilibrium states of irrotational binary neutron stars as the initial condition.

#### ACKNOWLEDGMENTS

The author thanks T. Baumgarte, Y. Kojima, T. Nakamura, K. Oohara, L. Rezzolla, M. Sasaki, and S. Shapiro for helpful conversations and discussions. He also thanks T. Baumgarte and L. Rezzolla for reading this manuscript and providing valuable comments. Numerical computations were performed on the FACOM VPP 300R and VX/4R machines in the data processing center

of the National Astronomical Observatory of Japan. This work was supported by a Grant-in-Aid (Nos. 08NP0801 and 09740336) of the Japanese Ministry of Education, Science, Sports and Culture, and JSPS Fellowships for Research Abroad.

#### APPENDIX A: NUMERICAL METHOD FOR SOLVING HYDRODYNAMIC EQUATIONS

To compute the advection in the hydrodynamic equations, in this paper, we use the second order scheme by van Leer [51] as Oohara and Nakamura used in their works [14,52] or as we used in a semi relativistic simulation [53]. As we have shown in Sec. III and IV, it is possible to perform simulations of many interesting problems stably and fairly accurately for several dynamical timescales using this scheme. If we are interested in problems in which shocks play a very important role, we should use one of the modern shock-capturing schemes as adopted in [15,54]. However, in coalescences of binary neutron stars, it seems that shocks do not play a crucially important role and that they do not change the results drastically [12]. We expect that the method employed here is suitable for our purpose, although there is still room for further improvement.

Since we solve the entropy equation instead of the energy equation, it is impossible to capture shocks without adding artificial viscosity. Hence, we add an artificial viscosity using a method similar to that adopted by Hawley, Smarr and Wilson [55]. The following artificial viscosity was included only in the case when we studied merger of binary neutron stars.

For simplicity, we include the artificial viscosity like a bulk viscosity and it consequently appears in the evolution equation where the pressure does. As the form of the viscous pressure, we choose

$$P_{\text{vis}} = \begin{cases} C_{\text{vis}} \frac{e_*^\Gamma}{(we^{6\phi})^{\Gamma-1}} (\delta v)^2 & \text{for } \delta v < 0, \\ 0 & \text{for } \delta v \geq 0, \end{cases} \quad (\text{A1})$$

where  $\delta v = 2\delta x \partial_k v^k$  and  $C_{\text{vis}}$  is a constant which we phenomenologically set below.

When including the artificial viscosity, we change the pressure gradient term  $\partial_k P$  in the right-hand side of Eq. (2.10) into  $\partial_k(P + P_{\text{vis}})$ . If we simply regard  $P_{\text{vis}}$  as an additional pressure, we should add the following term to the right-hand side of Eq. (2.11):

$$-\frac{1}{\Gamma}(\rho\epsilon)^{-1+1/\Gamma}P_{\text{vis}}[\partial_t(w e^{6\phi}) + \partial_k(w e^{6\phi} v^k)]. \quad (\text{A2})$$

However, as pointed out by Hawley et al. [55], the first term, which includes a time derivative, could cause a numerical instability. Hence, we neglect the first term, and only include the second one.

$C_{\text{vis}}$  is determined in a phenomenological manner. In merger of binary neutron stars, two neutron stars of nearly equal mass finally collide and a shock will be produced. The situation may be crudely compared with the 1D wall shock problem in which we consider the evolution of a fluid that initially has a uniform density and pressure, but a velocity field as

$$v^x = \begin{cases} V_0 & \text{for } x < 0, \\ -V_0 & \text{for } x > 0, \end{cases} \quad (\text{A3})$$

where  $V_0$  is a positive constant, and  $v^y = v^z = 0$ . The solution of the 1D wall shock problem in special relativity can be analytically calculated. We have performed test simulations of this problem, and the value of  $C_{\text{vis}}$  which well reproduces the analytical solution was used in numerical computations.

To mimic the collision of two neutron stars, we set initial conditions as  $V_0 = 0.1 - 0.4$  and  $P/\rho = 0.1$  for the test. In Fig. 31, we show the results for  $V_0 = 0.4$  and  $C_{\text{vis}} = 10$  at  $t = 0.4$ . In this test, we set  $\rho = 1$  and  $\delta x = 0.005$ . The solid lines denote the analytical solution, and the open circles are the numerical results. Although well known spurious oscillation of  $\rho$ ,  $P$ , and  $v^x$  is generated [55], the numerical results agree with the analytical solution fairly well.

## APPENDIX B: RADIAL OSCILLATION PERIOD OF SPHERICAL STARS

We estimate an approximate radial oscillation period of spherical stars using the method presented by Chandrasekhar [28].

If we write the line element as

$$ds^2 = -e^\nu dt^2 + e^\Phi d\bar{r}^2 + \bar{r}^2 d\Omega, \quad (\text{B1})$$

then the angular frequency  $\sigma$  of the radial oscillation for a polytropic star of radius  $R$  is written as [28]

$$\begin{aligned} \sigma^2 = & \left[ 4 \int_0^R e^{(\Phi+\nu)/2} \bar{r} \frac{dP}{d\bar{r}} \xi^2 d\bar{r} \right. \\ & + \int_0^R e^{(\Phi+3\nu)/2} \frac{\Gamma P}{\bar{r}^2} \left\{ \frac{d}{d\bar{r}} (\bar{r}^2 e^{-\nu/2} \xi) \right\}^2 d\bar{r} \\ & - \int_0^R e^{(\Phi+\nu)/2} \left( \frac{dP}{d\bar{r}} \right)^2 \frac{\bar{r}^2 \xi^2}{\rho h} d\bar{r} \\ & \left. + 8\pi \int_0^R e^{(3\Phi+\nu)/2} \rho P h \bar{r}^2 \xi^2 d\bar{r} \right] \\ & \times \left[ \int_0^R e^{(3\Phi-\nu)/2} \rho h \bar{r}^2 \xi^2 d\bar{r} \right]^{-1}, \end{aligned} \quad (\text{B2})$$

where  $\xi$  denotes the  $\bar{r}$ -component of the Lagrangian displacement. If we substitute an eigenfunction  $\xi$  for the eigenvalue equation, we can obtain a correct  $\sigma$ . Here, we evaluate  $\sigma$  approximately by substituting a trial eigenfunction for  $\xi$  without solving an eigenvalue equation for  $\xi$ . Following Chandrasekhar [28], we substitute the approximate eigenfunctions as

$$\xi = \bar{r} e^{b\nu}, \quad (\text{B3})$$

where  $b$  is a constant. In Fig. 32, we show  $\sigma \rho_c^{-1/2}$  as a function of  $\rho_c$  for polytropic star of  $(\Gamma, K) = (5/3, 10)$  and  $(2, 200/\pi)$  for  $b = 0$  (the solid line),  $1/2$  (the dashed line) and  $-1/2$  (the long dashed line). We note that beyond a critical density,  $\sigma^2$  becomes negative in each model, implying that the star becomes unstable for some oscillation modes. Even though we use the trial function for  $\xi$ , we can approximately find the real critical points of stability ( $\rho_c \sim 1.85 \times 10^{-3}$  for  $\Gamma = 5/3$  and  $\sim 5.0 \times 10^{-3}$  for  $\Gamma = 2$ ). We also find that the oscillation frequency in the Newtonian limit ( $\rho_c \rightarrow 0$ ) agrees well with that obtained in the Newtonian theory ( $\sigma \rho_c^{-1/2} = 1.377$  for  $\Gamma = 5/3$ , and  $2.187$  for  $\Gamma = 2$  [56]). Thus, we can recognize that this approximate method is fairly reliable for estimating  $\sigma$  approximately.

From the figure, we can judge  $\sigma \sim 0.60 \rho_c^{1/2}$  for  $(\Gamma, \rho_c) = (5/3, 10^{-3})$  and  $\sigma \sim 0.91 \rho_c^{1/2}$  for  $(\Gamma, \rho_c) =$

$(2,3 \times 10^{-3})$ , and the resulting oscillation periods are  $\sim 10.5\rho_c^{-1/2}$  and  $\sim 6.9\rho_c^{-1/2}$ , respectively. These are in good agreement with the numerical results in Sec. III.B and III.C.

---

[1] A. Abramovici, et al. *Science* **256**, 325 (1992).

[2] K. S. Thorne, in *Proceeding of Snowmass 95 Summer Study on Particle and Nuclear Astrophysics and Cosmology*, eds. E. W. Kolb and R. Peccei (World Scientific, Singapore, 1995), p. 398.

[3] C. Bradaschia, et al. *Nucl. Instrum. and Methods* **A289**, 518 (1990).

[4] J. Hough, in *Proceedings of the Sixth Marcel Grossmann Meeting*, edited by H. Sato and T. Nakamura (World Scientific, Singapore, 1992), p. 192.

[5] K. Kuroda, et al. in *Proceedings of International Conference on Gravitational Waves: Sources and Detectors*, edited by I. Ciufolini and F. Fidecaro (World Scientific, Singapore, 1997), p. 100.

[6] For example, L. Blanchet, in *Relativistic gravitation and gravitational radiation*, edited by J.-P. Lasota and J.-A. Marck (Cambridge University Press, Cambridge, 1997), p. 33: See also references cited therein.

[7] S. Bonazzolla, E. Gourgoulhon, and J.-A. Marck, *Phys. Rev. D* **58**, 104020 (1998): *Phys. Rev. Lett.* **82**, 892 (1999): in *proceeding of 19th Texas symposium on relativistic astrophysics*, to be published (gr-qc/9904040).

[8] K. Uryu, in *proceeding of 19th Texas symposium on relativistic astrophysics*, to be published.

[9] P. Maronetti, G. J. Mathews and J. Wilson, to be published in *Phys. Rev. D* (gr-qc/9906088).

[10] For example, R. Narayan, B. Paczynski, and T. Piran, *Astrophys. J.* **395**, L83 (1992):  
M. J. Rees, in *proceeding of eighteenth Texas symposium on relativistic astrophysics, and cosmology*, eds. A. V. Olinto, J. A. Frieman, and D. N. Schramm (World Scientific), p. 34:  
P. Meszaros, astro-ph/9904038.

[11] M. R. Metzger et al., *Nature* **387**, 878 (1997):  
S. R. Kulkarni et al., *Nature* **393**, 35 (1998).

[12] For example, M. Ruffert, H.-Th. Janka, and G. Schäfer, *Astron. and Astrophys.* **311**, 532 (1996):  
M. Ruffert and H.-Th. Janka, *Astron. and Astrophys.* **344**, 573 (1999): See also references cited therein.

[13] T. Nakamura, K. Oohara, and Y. Kojima, *Prog. Theor. Phys. supplement* **90**, 76 (1987):  
T. Nakamura and K. Oohara, in *Frontiers in Numerical Relativity*, eds. C. R. Evans, L. S. Finn, and D. W. Hobill (Cambridge University Press, 1989), p. 254.

[14] K. Oohara and T. Nakamura, in [6], p. 309.

[15] J. A. Font, M. Miller, W.-M. Suen, and M. Tobias, gr-qc/9811015: M. Miller, W.-M. Suen and M. Tobias, gr-qc/9904041.

[16] M. Shibata, *Prog. Theor. Phys.* **101**, 1199 (1999).

[17] M. Shibata and T. Nakamura, *Phys. Rev. D* **52**, 5428 (1995).

[18] M. Shibata, *Prog. Theor. Phys.* **101**, 251 (1999).

[19] The idea that  $F_i$  should be defined and evolved to maintain the stability of numerical system was already suggested by T. Nakamura more than 10 years ago (see [13]).

[20] L. Smarr and J. W. York, *Phys. Rev. D* **17**, 1945 (1978): Note that the definition of the minimum distortion gauge condition in this paper is slightly different from the original version by Smarr and York.

[21] For example, N. T. Bishop et al., gr-qc/9801070, and references cited therein.  
L. Rezzolla et al., *Phys. Rev. D* **59**, 064001 (1998).

[22] R. F. Stark and T. Piran, *Comp. Phys. Rep.* **5**, 221 (1987).

[23] W. H. Press, B. P. Flannery, S. A. Teukolsky, and W. T. Vetterling, *Numerical Recipes* (Cambridge University Press, 1989).

[24] T. W. Baumgarte et al., *Phys. Rev. D* **57**, 7299 (1998): See also references cited therein.

[25] H. Asada and M. Shibata, *Phys. Rev. D* **54**, 3762 (1996).

[26] M. Berger and J. Oliger, *J. Comp. Phys.* **53**, 484 (1984).

[27] M. Shibata, T. W. Baumgarte, and S. L. Shapiro, submitted to *Phys. Rev. D*.

[28] S. Chandrasekhar, *Astrophys. J.* **140**, 417 (1964).

[29] In the final phase of these simulations, it is found that  $\rho$  decreases with time in the AMD gauge condition, while  $\rho_*$  increases. These incorrect solutions are due to the fact that  $\phi$  and  $\rho_*$  inaccurately increases (and hence  $\rho$  calculated from  $\rho_* e^{-6\phi}/w$  may decrease).

[30] Y. Kojima, *Prog. Theor. Phys.* **77**, 297 (1987), and also private communication. As far as the author knows, study on stellar pulsation is not done assuming an usual polytropic equation of state as  $P = K\rho^\Gamma$ , but done assuming a relativistic polytrope  $P = K(\rho + \rho\varepsilon)^\Gamma$ . Since the  $f$ -mode angular frequencies cited here are those of the relativistic polytrope, we expect that they are not equal to the  $f$ -mode frequencies of the usual polytrope. However, the difference is of  $O(\varepsilon)$  and the error on the magnitude of the oscillation frequency is expected not to be large. Actually, we have found that the configurations of stars of nearly equal  $M_g/R \sim 0.1$  but of different equations of state are quite similar. We expect that the value cited here will be valid within  $\sim 10\%$  error for stars of  $M_g/R = O(1/10)$ .

[31] K. D. Kokkotas, in [6], p. 89.

[32] G. Cook, S. L. Shapiro, and S. A. Teukolsky, *Phys. Rev. D* **53**, 5533 (1996).

[33] The numerical solutions for rigidly rotating stars are obtained using a method employed in the following paper: M. Shibata and M. Sasaki, *Phys. Rev. D* **58**, 104011 (1998).

[34] M. Shibata, *Phys. Rev. D* **55**, 6019 (1997).

[35] In Newtonian and post Newtonian simulations, we have also faced a small amount of numerical dissipation of the angular momentum, which affects the evolution of the binary slightly: For example, M. Shibata, K. Oohara and T. Nakamura, *Prog. Theor. Phys.* **98**, 1081 (1997).

[36] L. Blanchet, B. R. Iyer, C. M. Will and A. G. Wiseman, *Class. Quant. Grav.* **13**, 575 (1996).

- [37] For example, S. L. Shapiro and S. A. Teukolsky, *Black Holes, White Dwarfs, and Neutron Stars* (New York, Wiley, 1983), chapter 16.
- [38] As for numerical results and arguments for supramassive stars, see for example, G. Cook, S. L. Shapiro, and S. A. Teukolsky, *Astrophys. J.* **422**, 227 (1994).
- [39] G. Cook, S. L. Shapiro, and S. A. Teukolsky, *Astrophys. J. Lett.* **423**, L117 (1994).
- [40] N. Stergioulas and J. L. Friedman, *Astrophys. J.* **492**, 301 (1998).
- [41] T. W. Baumgarte and S. L. Shapiro, *Astrophys. J.* **504**, 431 (1998).
- [42] J. O. Goussard, P. Haensel and J. L. Zdunik, *Astron. Astrophys.* **321**, 822 (1997).
- [43] E. Flowers and N. Itoh, *Astrophys. J.* **206**, 218 (1976); **230**, 847 (1979);  
C. Cutler and L. Lindblom, *Astrophys. J.* **314**, 234 (1987).
- [44] In [37], chapter 10.
- [45] In [37], chapter 11.
- [46] S. A. Balbus and J. F. Hawley, *Rev. Mod. Phys.* **70**, 1 (1998).
- [47] N. Andersson, *Astrophys. J.* **502**, 708 (1998);  
J. L. Friedman and S. M. Morsink, *Astrophys. J.* **502**, 714 (1998).  
B. J. Owen et al., *Phys. Rev. D* **58**, 084020 (1998).
- [48] For example, S. Detweiler and L. Lindblom, *Astrophys. J.* **213**, 197 (1977).  
D. Lai and S. L. Shapiro, *Astrophys. J.* **442**, 259 (1995).
- [49] M. Shibata and K. Uryu, in preparation.
- [50] C. S. Kochanek, *Astrophys. J.* **398**, 234 (1992);  
L. Bildsten and C. Cutler, *Astrophys. J.* **400**, 175 (1992).
- [51] B. J. van Leer, *J. Comp. Phys.* **23**, 276 (1977).
- [52] K. Oohara and T. Nakamura, *Prog. Theor. Phys.* **82**, 535 (1989); See appendix A of this paper as for the handling of the advection terms in the present paper.
- [53] M. Shibata, T. W. Baumgarte, and S. L. Shapiro, *Phys. Rev. D* **58**, 023002 (1998).
- [54] For example, J. A. Pons, J. A. Font, J. M. Ibanez, J. M. Marti and J. A. Miralles, *Astron. Astrophys.* **339**, 638 (1998) and references cited therein.
- [55] J. F. Hawley, L. L. Smarr, and J. M. Wilson, *Astrophys. J. Supplement Series* **55**, 211 (1984).
- [56] J. P. Cox, *Theory of Stellar Pulsation* (Princeton University Press, 1980), p. 106;  
S. L. Shapiro, personal communication.

**Table I.** The list of the central density  $\rho_c$ , total rest mass  $M_*$ , gravitational mass  $M_g$ ,  $J/M_g^2$ , and rotation period  $P$  for rotating neutron stars of  $\Gamma = 5/3$  and 2 at mass-shedding limits.

$\rho_c$	$M_*$	$M_g$	$J/M_g^2$	$P$	$\Gamma$
$9.94 \times 10^{-4}$	1.67	1.60	0.427	397	$5/3$
$2.77 \times 10^{-3}$	1.58	1.45	0.598	163	2

**Table II.** The list of the maximum density, total rest mass  $M_*$ , gravitational mass  $M_g$ ,  $J/M_g^2$ , coordinate separation  $a$ , orbital period  $P$ , and ratio of the emission timescale of gravitational waves to the orbital period  $R_\tau$  for corotating binary neutron stars in approximate quasi-equilibrium states.

$\rho_{\max}$	$M_*$	$M_g$	$J/M_g^2$	$a$	$P$	$R_\tau$
$6 \times 10^{-4}$	2.84	2.72	1.20	38.3	902	9.2
$10^{-3}$	3.07	2.92	1.11	32.9	694	5.3

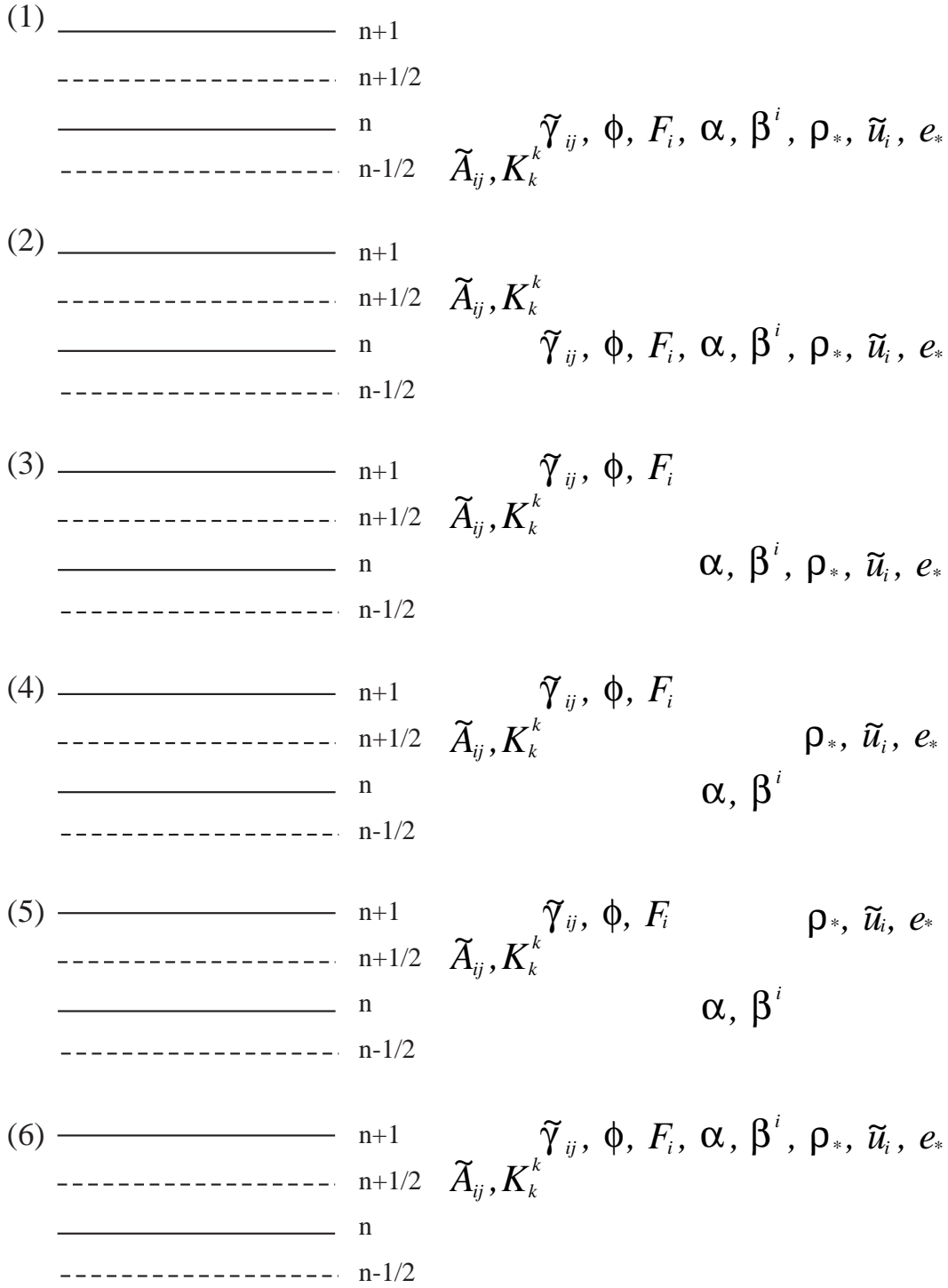


FIG. 1. Schematic picture for a numerical scheme of time evolution of variables from  $n$ -th to  $(n + 1)$ -th time step.

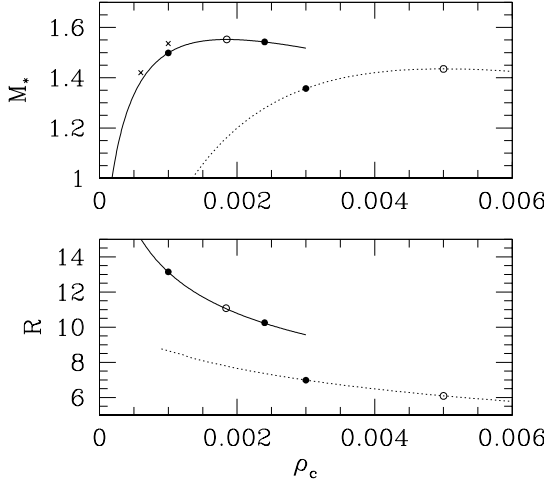


FIG. 2. Rest mass  $M_*$  and circumferential radius  $R$  as a function of central density  $\rho_c$  for spherical polytropic stars of  $K = 10$  and  $\Gamma = 5/3$  (solid lines) and of  $K = 200/\pi$  and  $\Gamma = 2$  (dotted lines). The filled circles denote the equilibrium stars which are used in test simulations (the tests 2 and/or 3), and the open circles denote the critical configuration of stability against gravitational collapse. The cross in the figure for  $M_*$  –  $\rho_c$  denotes the relation between  $M_*/2$  and the maximum density for corotating binary neutron stars in approximate quasi-equilibrium states which are adopted as initial conditions in Sec. III.E and IV.

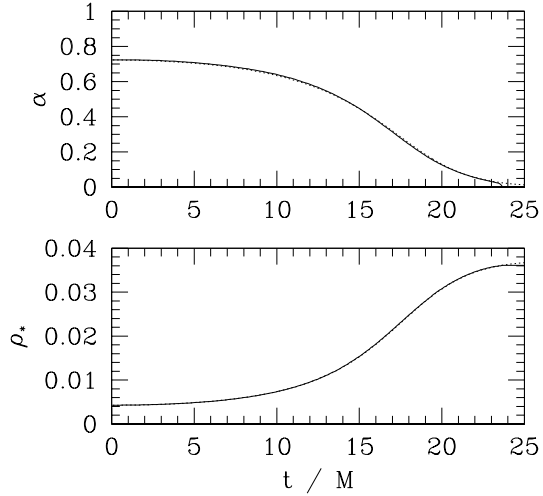


FIG. 3.  $\alpha$  and  $\rho_*$  at  $r = 0$  as a function of time for a spherical dust collapse with zero shift gauge condition. The dotted lines are the 1D results, and the solid lines are the 3D results.

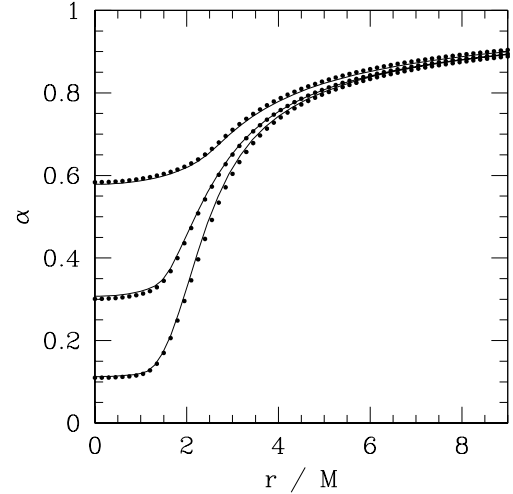


FIG. 4.  $\alpha$  along the  $x$ -axis at selected times ( $t = 12.0, 17.2$ , and  $20.4$ ) for a spherical dust collapse with zero shift gauge condition for the 1D results (the solid lines) and 3D results (the filled circles).

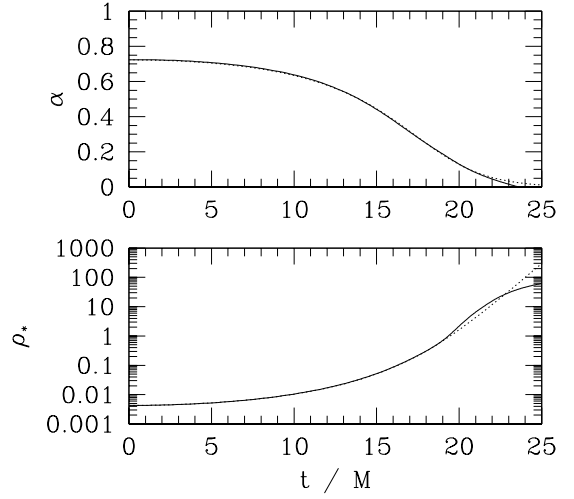


FIG. 5. The same as Fig. 3, but with the MD (or AMD) gauge condition. The dotted and solid lines denote the 1D and 3D results, respectively.

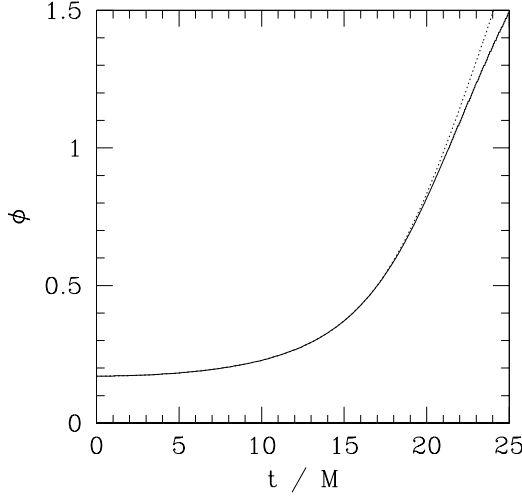


FIG. 6.  $\phi$  as a function of time for a spherical dust collapse in the MD (or AMD) gauge condition. The dotted and solid lines denote the 1D and 3D results, respectively.

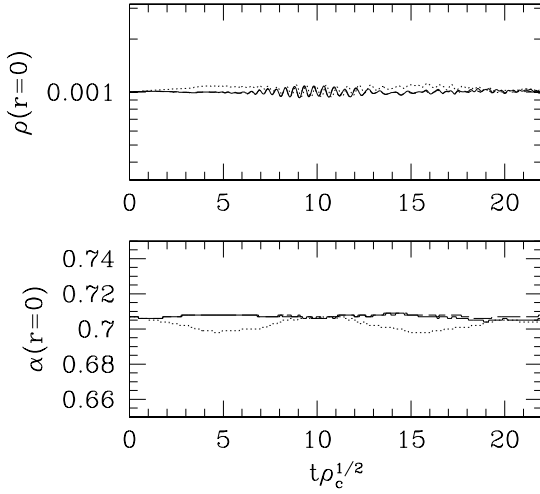


FIG. 7.  $\rho$  and  $\alpha$  at  $r = 0$  as a function of time ( $t\rho_c^{1/2}$ ) in 3D numerical evolution of a stable spherical polytropic star of  $\rho_c = 10^{-3}$ ,  $K = 10$  and  $\Gamma = 5/3$ . The solid and dotted lines denote the results in zero shift gauge condition, and the dashed line in the AMD gauge condition. In the simulation shown with the dotted line, we reduce  $K$  by a factor 0.5% initially, and in other cases, we give equilibrium states without any perturbation.

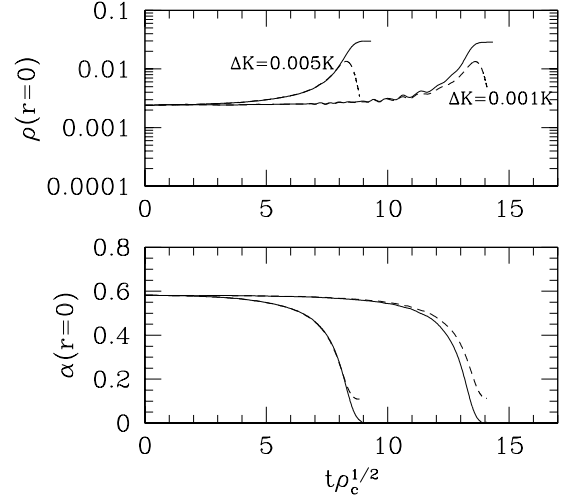


FIG. 8.  $\rho$  and  $\alpha$  at  $r = 0$  as a function of time ( $t\rho_c^{1/2}$ ) in 3D numerical evolution of an unstable spherical polytropic star of  $\rho_c = 2.4 \times 10^{-3}$ ,  $K = 10$  and  $\Gamma = 5/3$ . The solid and dashed lines denote the results in the zero shift gauge and AMD gauge conditions, respectively. In these simulations, we reduce  $K$  by a factor 0.1% or 0.5% initially.

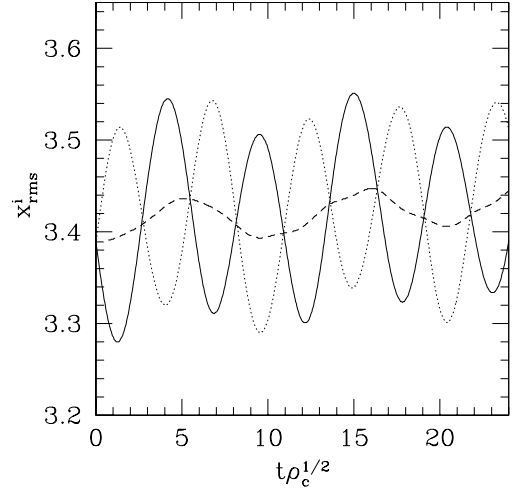


FIG. 9.  $x_rms^i$  and  $\alpha$  at  $r = 0$  as a function of time ( $t\rho_c^{1/2}$ ) for a perturbed spherical star of  $\rho_c = 10^{-3}$ ,  $K = 10$  and  $\Gamma = 5/3$  with a quadrupole perturbation of + mode. The solid, dotted and dashed lines denote  $x_{rms}$ ,  $y_{rms}$ , and  $z_{rms}$ , respectively.

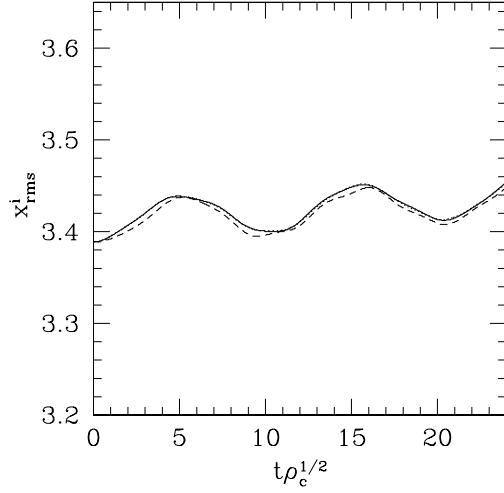


FIG. 10. The same as Fig. 9, but for  $\times$  mode perturbation

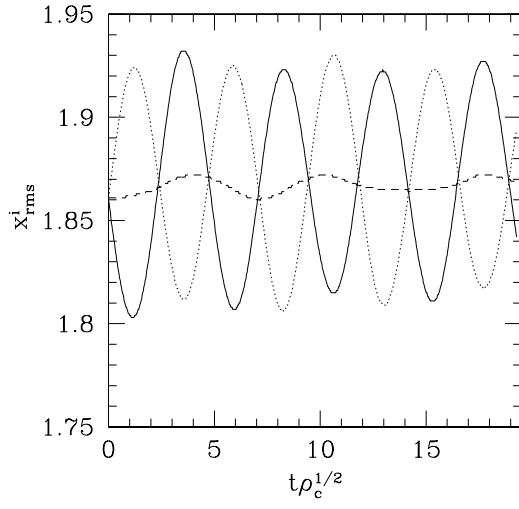


FIG. 11. The same as Fig. 9, but for  $\rho_c = 3 \times 10^{-3}$ ,  $\Gamma = 2$ , and  $K = 200/\pi$ .

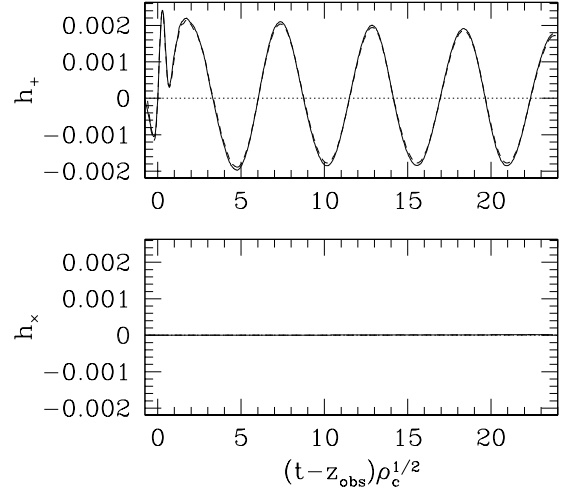


FIG. 12.  $h_+$  and  $h_x$  as a function of a retarded time for a perturbed spherical star of  $\rho_c = 10^{-3}$ ,  $K = 10$  and  $\Gamma = 5/3$  with a quadrupole perturbation of  $+$  mode. The solid and dashed lines denote those extracted at  $z_{\text{obs}} = 24.5$  and  $19.5$ , respectively.

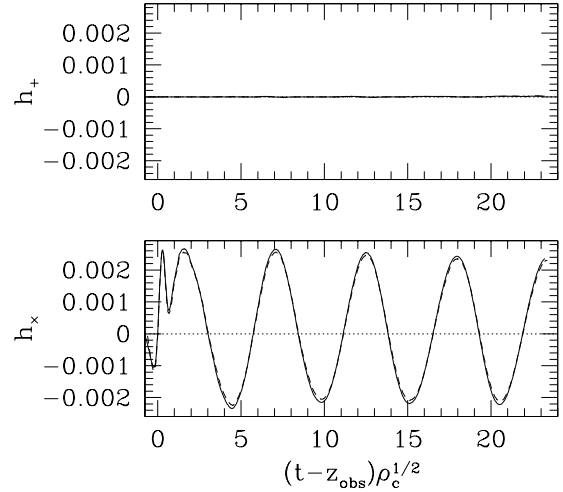


FIG. 13. The same as Fig. 12, but for  $\times$  mode perturbation.

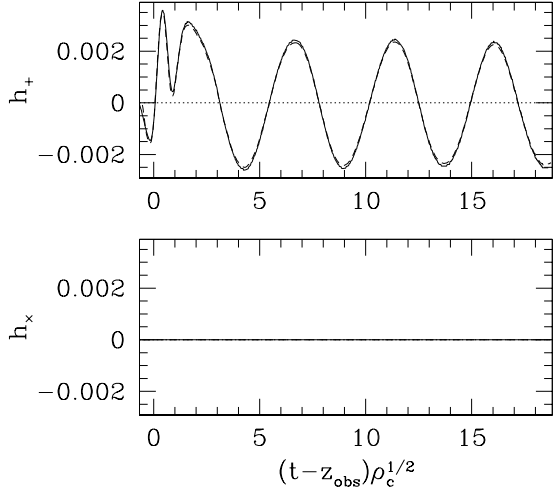


FIG. 14. The same as Fig. 12, but for  $\rho_c = 3 \times 10^{-3}$ ,  $\Gamma = 2$ , and  $K = 200/\pi$ .

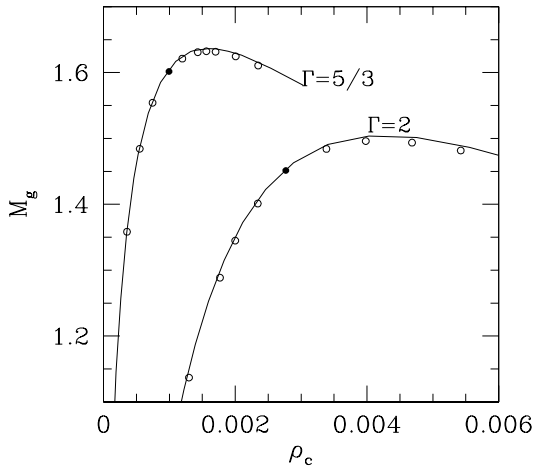


FIG. 15. The gravitational mass as a function of  $\rho$  at  $r = 0$  ( $\rho_c$ ) for rotating stars of  $\Gamma = 5/3$  and  $K = 10$ , and  $\Gamma = 2$  and  $K = 200/\pi$ . The solid lines denote rotating stars at mass-shedding limits obtained from exact equations. The open and filled circles denote rotating stars at mass-shedding limits obtained using a conformal flatness approximation. The rotating stars we use in this paper are marked with the filled circles.

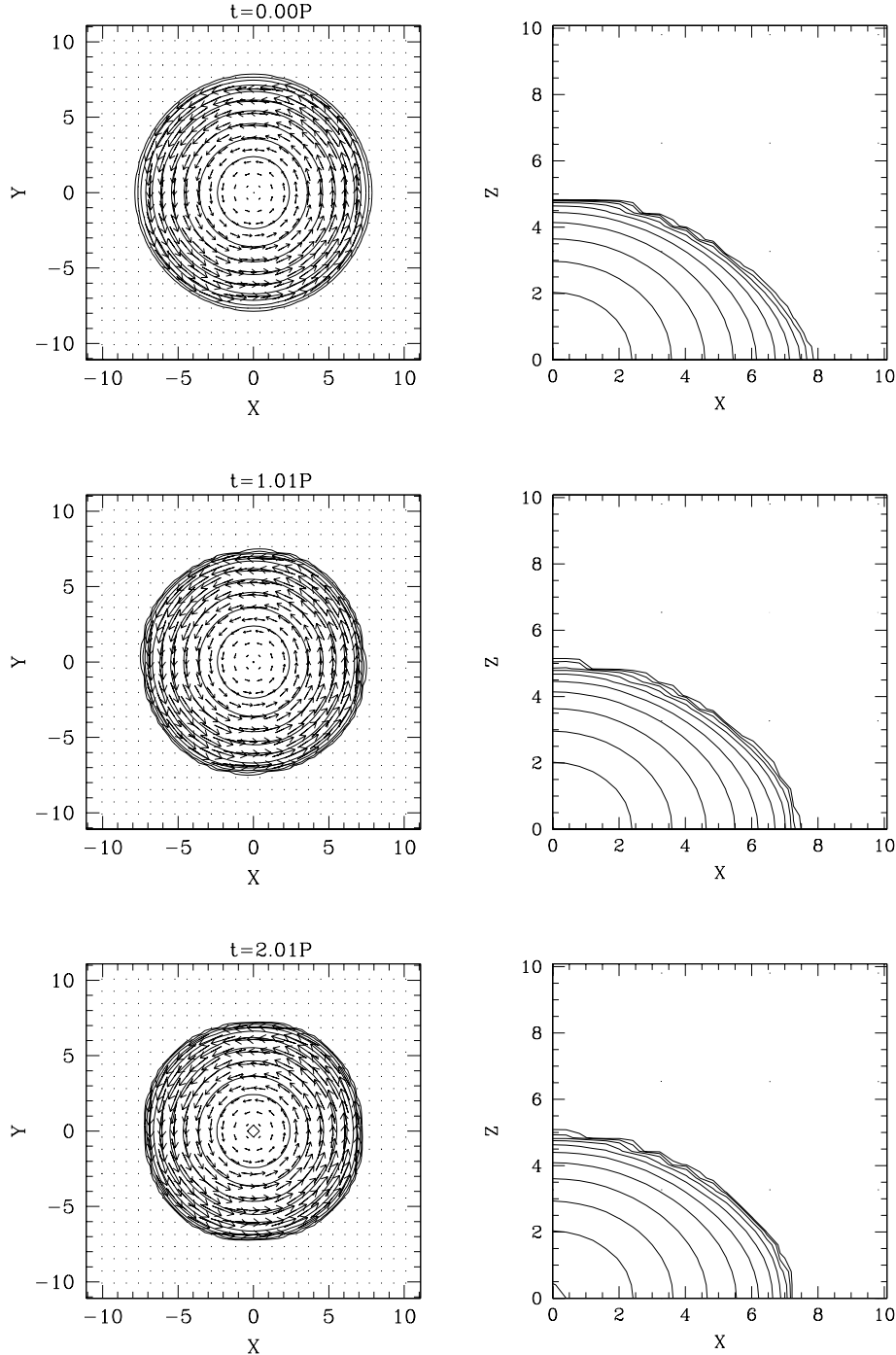


FIG. 16. Snapshots of the density contour lines for  $\rho_*$  and the velocity flow for  $(v^x, v^y)$  in the equatorial plane (left) and in the  $y = 0$  plane (right) for a rotating star at the mass-shedding limit and  $\Gamma = 2$  at selected times. The contour lines are drawn for  $\rho_*/\rho_{*c} = 10^{-0.3j}$ , where  $\rho_{*c} = 0.0122$  denotes  $\rho_*$  at  $r = 0$  and  $t = 0$ , for  $j = 0, 1, 2, \dots, 10$ . Vectors indicate the local velocity field and the maximum length denotes  $\sim 0.26c$ .

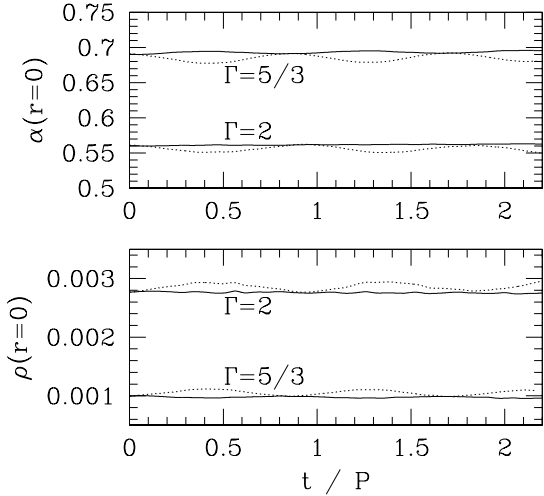


FIG. 17.  $\alpha$  and  $\rho (= \rho_* e^{-6\phi}/w)$  at  $r = 0$  as a function of  $t/P$  for  $\Gamma = 5/3$  and 2. The solid and dotted lines denote the results for initial conditions in which no perturbation is added and the pressure is depleted, respectively.

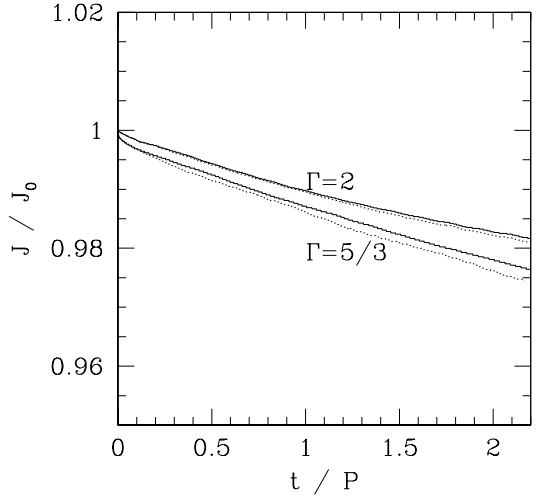


FIG. 19. The same as Fig. 17, but for  $J/J_0$  as a function of  $t/P$ .

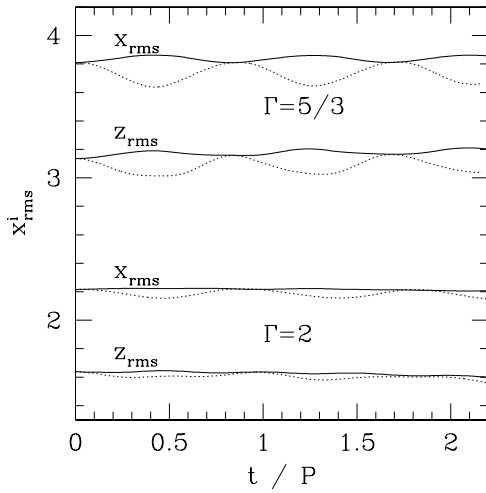


FIG. 18. The same as Fig. 17, but for  $x_{\text{rms}}$  and  $z_{\text{rms}}$  as a function of  $t/P$ .

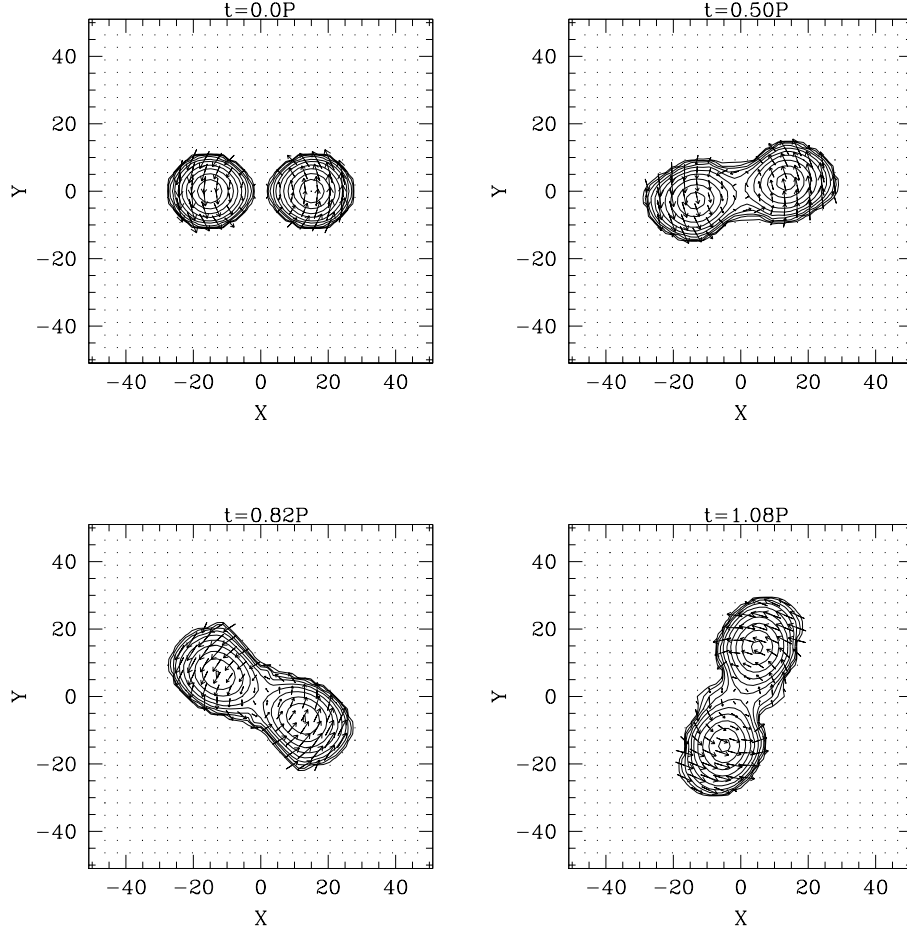


FIG. 20. Snapshots of the density contour lines for  $\rho_*$  and the velocity flow for  $(v^x, v^y)$  in the equatorial plane for a corotating binary neutron star of  $\Gamma = 5/3$  in nearly quasi-equilibrium states. The contour lines are drawn for  $\rho_*/\rho_{* \text{ max}} = 10^{-0.3j}$ , where  $\rho_{* \text{ max}} = 0.00305$  denotes the maximum value of  $\rho_*$  at  $t = 0$ , for  $j = 0, 1, 2, \dots, 10$ . Vectors indicate the local velocity field and the maximum length denotes  $\sim 0.23c$ .

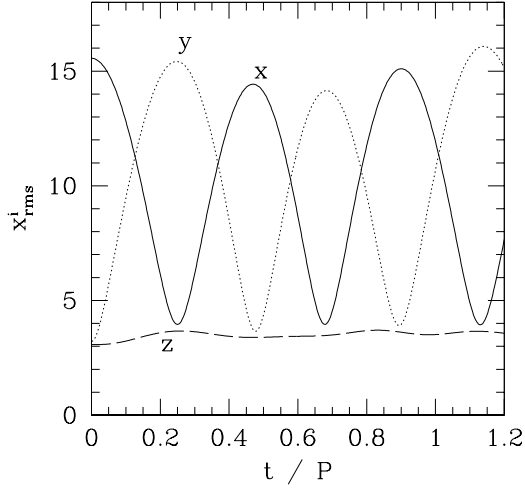


FIG. 21.  $x_{\text{rms}}^i$  as a function of  $t/P$  of a corotating binary neutron star in an approximate quasi-equilibrium state. The solid, dotted and dashed lines denote  $x_{\text{rms}}$ ,  $y_{\text{rms}}$ , and  $z_{\text{rms}}$ .

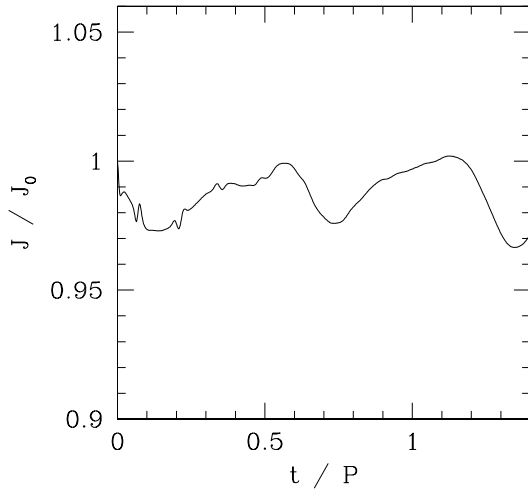


FIG. 22.  $J/J_0$  as a function of  $t/P$  of a corotating binary neutron star in an approximate quasi-equilibrium state.

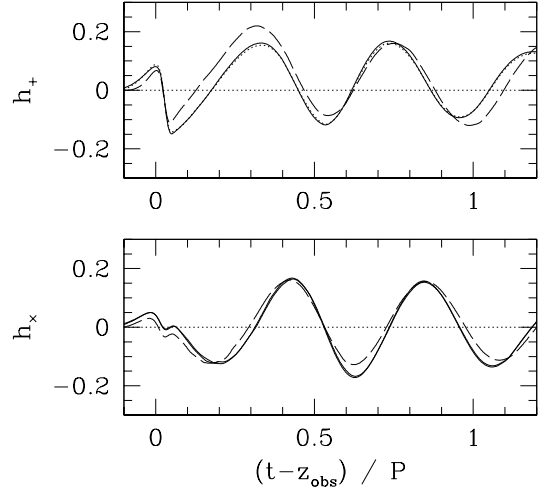


FIG. 23.  $h_+$  and  $h_x$  as a function of a retarded time of a corotating binary neutron star in an approximate quasi-equilibrium state. The solid and dotted lines denote those extracted at  $z_{\text{obs}} = 106.6$  and  $85.3$  for  $N = 116$ , respectively, and the dashed lines those extracted at  $z_{\text{obs}} = 69.5$  for  $N = 76$ .

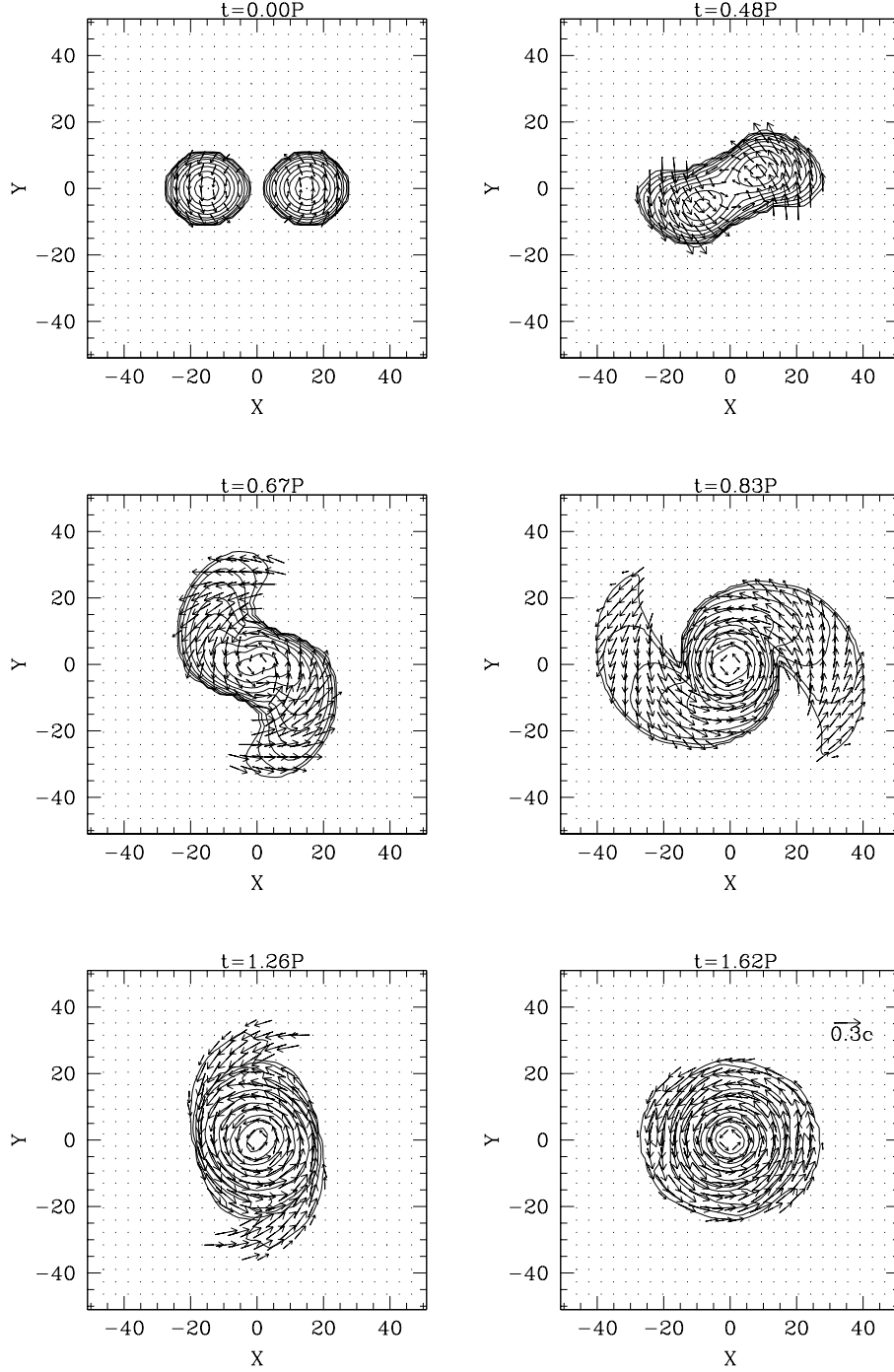


FIG. 24. Snapshots of the density contour lines for  $\rho_*$  and the velocity flow for  $(v^x, v^y)$  in the equatorial plane for a corotating binary neutron star of  $\Gamma = 5/3$  and  $\rho_{\max}(t = 0) = 10^{-3}$  for a merging case. The contour lines are drawn for  $\rho_*/\rho_{* \max} = 10^{-0.3j}$ , where  $\rho_{* \max} = 0.00305$ , for  $j = 0, 1, 2, \dots, 10$ . Vectors indicate the local velocity field and the length is shown in normalization of  $0.3c$ . At  $t = 1.62P$ ,  $\rho_{* \max} \simeq 0.011$  and  $\rho_{\max} \simeq 0.0014$ , respectively.

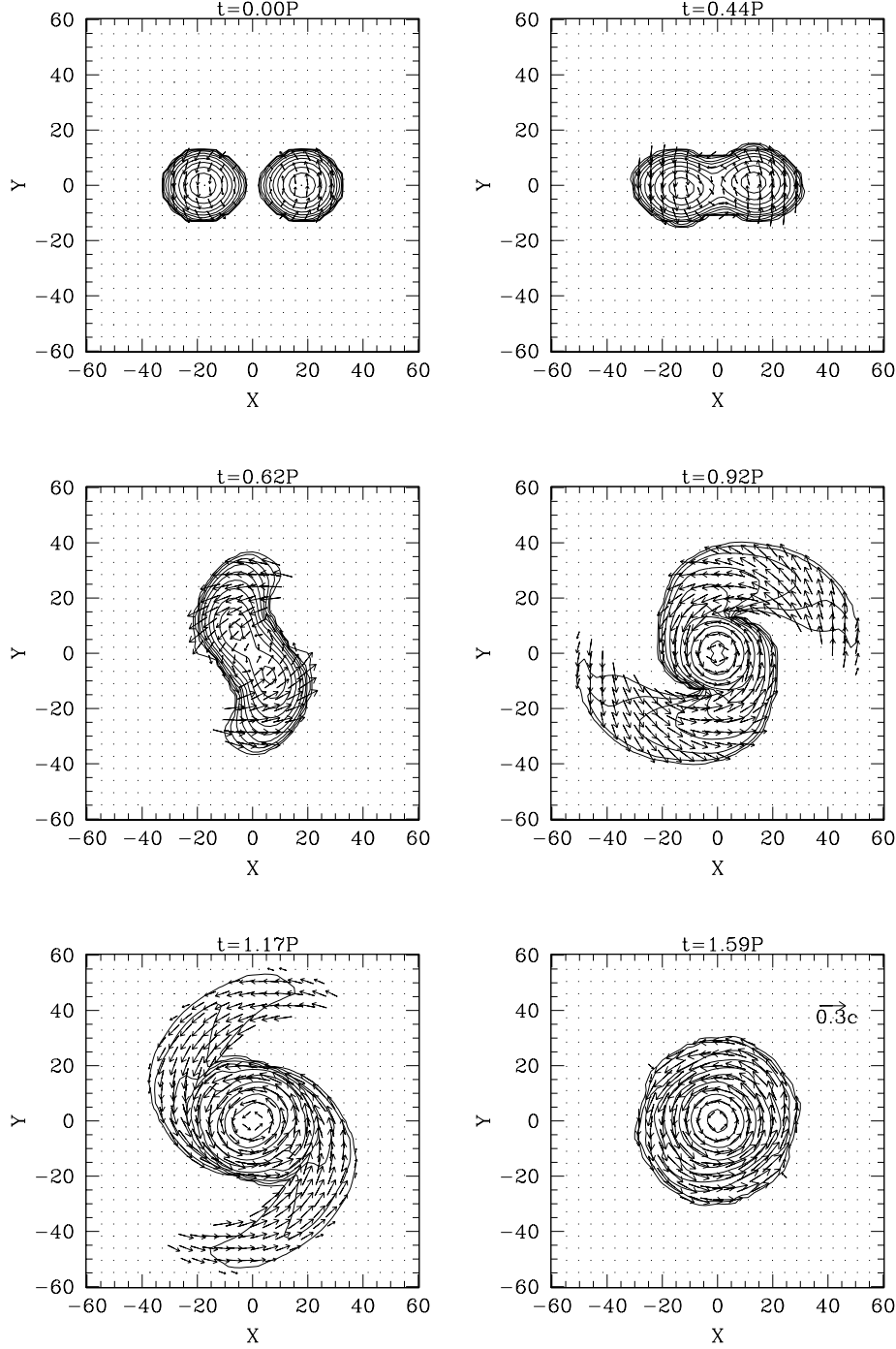


FIG. 25. The same as Fig. 24, but for  $\rho_{\max}(t=0) = 6 \times 10^{-4}$ . The contour lines are drawn for  $\rho_*/\rho_{* \max} = 10^{-0.3j}$ , where  $\rho_{* \max} = 0.00143$ , for  $j = 0, 1, 2, \dots, 10$ . At  $t = 1.59P$ ,  $\rho_* \simeq 0.0019$  and  $\rho_{\max} \simeq 6 \times 10^{-4}$ , respectively.

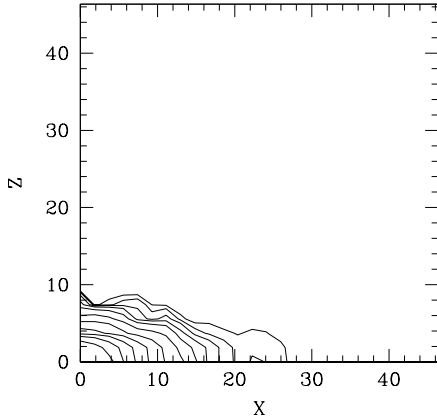


FIG. 26. The density contour lines for  $\rho_*$  in the  $y = 0$  plane after merger ( $t = 1.62P$ ) of a corotating binary neutron star of  $\Gamma = 5/3$  and  $\rho_{\max}(t = 0) = 10^{-3}$ . The contour lines are drawn for  $\rho_*/\rho_{* \max} = 10^{-0.3j}$ , where  $\rho_{* \max} = 0.00305$  denotes  $\rho_*$  at  $r = 0$  and  $t = 0$ , for  $j = 0, 1, 2, \dots, 10$ .

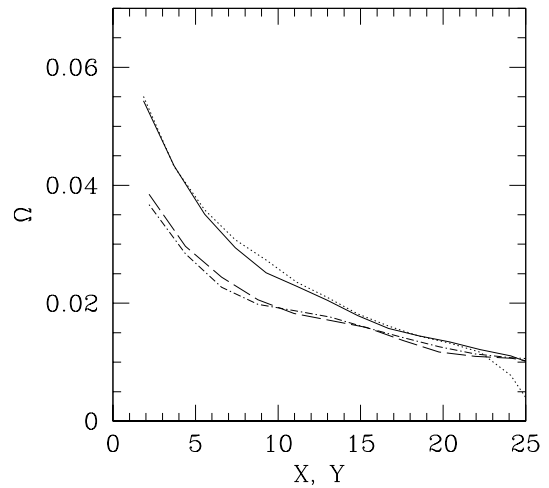


FIG. 28. The angular velocity along the  $x$ -axis (the solid line) and  $y$ -axis (the dotted line) at  $t = 1.62P$  for  $\rho_{\max}(t = 0) = 10^{-3}$  and along the  $x$ -axis (the dashed line) and  $y$ -axis (the dotted-dashed line) at  $t = 1.59P$  for  $\rho_{\max}(t = 0) = 6 \times 10^{-4}$ .

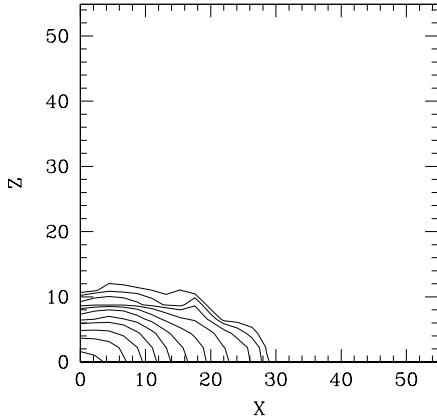


FIG. 27. The same as Fig. 26, but for  $\rho_{\max}(t = 0) = 6 \times 10^{-4}$  at  $t = 1.59P$ . The contour lines are drawn for  $\rho_*/\rho_{* \max} = 10^{-0.3j}$ , where  $\rho_{* \max} = 0.00143$ , for  $j = 0, 1, 2, \dots, 10$ .

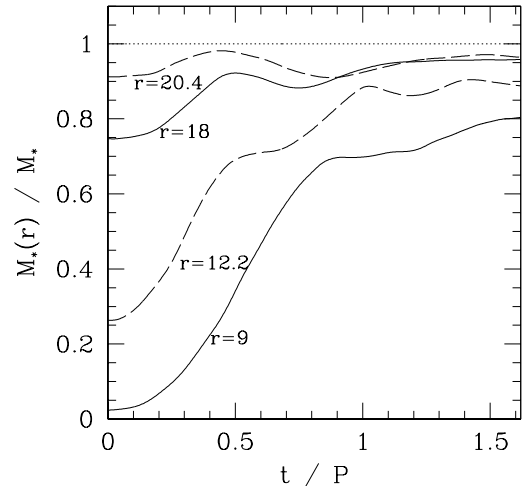


FIG. 29. Fraction of the rest mass inside a coordinate radius  $r$  as a function of  $t/P$  for  $\rho_{\max}(t = 0) = 10^{-3}$  (the solid lines) and  $6 \times 10^{-4}$  (the dashed lines).

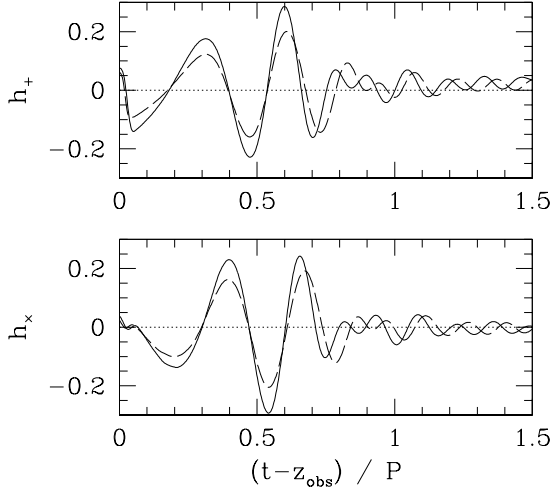


FIG. 30.  $h_+$  and  $h_x$  as a function of retarded time in the merger of corotating binary neutron stars of  $\rho_{\max}(t=0) = 10^{-3}$  (the solid lines) and  $6 \times 10^{-4}$  (dashed lines).

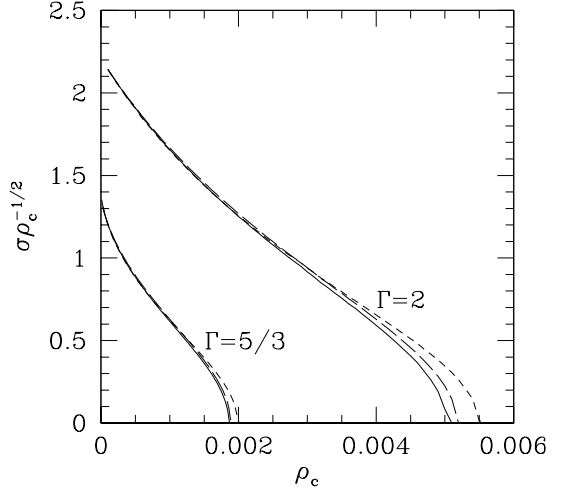


FIG. 32. The angular frequency ( $\sigma\rho_c^{-1/2}$ ) of the fundamental radial oscillation as a function of the central density for spherical polytropic stars of  $(K, \Gamma) = (10, 5/3)$  and  $(K, \Gamma) = (200/\pi, 2)$  with the trial functions of the Lagrangian displacement.

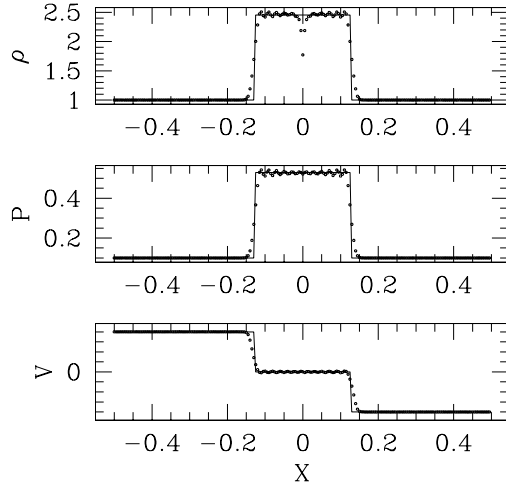


FIG. 31. Numerical results of  $\rho$ ,  $P$ , and  $v^x$  for the 1D wall shock problem in special relativity. The solid lines denote the exact solutions, and the open circles are numerical results.